Results of the *Telstar* Radiation Experiments

By W. L. BROWN, J. D. GABBE and W. ROSENZWEIG

(Manuscript received June 7, 1963)

The data from the particle experiments of the Telstar satellite have been analyzed to provide maps of the distribution of electrons and protons as measured in three of the Telstar detectors during the period from July through October, 1962. For the protons between 26 and 34 Mev and >50 Mev, the particle distributions are stable in time, but for the electron distribution there is a time decay of the electron flux over most of the region explored by the Telstar orbit. The connection of these observations to the high-altitude nuclear explosion of July 9, 1962, is discussed. The introduction of additional electrons by Russian tests at the end of October was also observed. The particle maps have been used to derive the integral particle exposure of the satellite, which is found to account quantitatively quite well for the radiation damage observed in the main solar power plant and in the radiation damage experiments on solar cells and special damage transistors carried by the satellite. In the main power plant the proton and electron contributions to damage are found to be equal. The integral particle exposure has also been used to compute the level of ionization in different depths of material in order to evaluate the degradation of semiconductor devices in the Telstar canister.

I. INTRODUCTION

This article presents some of the results obtained from the radiation experiments on the Telstar satellite. It describes the distribution of several classes of energetic charged particles mapped out by these experiments, and the integral radiation exposure of the satellite in orbit which has been calculated from these distributions. It also describes the radiation damage effects observed directly on semiconductor devices carried by the satellite and compares the damage with that to be expected on the basis of the orbital integrals.

1.1 *Charged Particle Experiment*

As described in detail in an accompanying article,[1] there are four silicon p-n junction charged particle detectors on the Telstar satellite, three that measure the distribution of protons in space at different energies and one that measures the electron distribution and some simple properties of the electron energy spectrum. All four detectors are energy proportional devices, giving an electrical pulse-height response proportional to the energy deposited by a charged particle in the active volume of the detector. By adjustment of the active volume, the levels of pulse height examined, and the amount of absorbing material which must be penetrated by a particle in reaching the detector, it is possible to distinguish protons from electrons and put bounds on the particle energies.

In the electron detector, particle pulses are sorted into four channels corresponding to deposition of different amounts of energy between 250 and 1000 Kev in the detector. Because of the nature of the energy loss processes for electrons, this detector primarily responds to electrons below 1 Mev but also responds to electrons of much higher energy with decreasing sensitivity. The efficiency of the four pulse-height channels of this detector for monoenergetic electrons in the region of primary sensitivity is shown in Fig. 1. The time and spatial variations of the electrons as observed by this detector will be discussed in considerable detail in Section 2.2. Electrons are of major importance in the radiation surface effects observed in the Telstar command decoder and also contribute about half of the radiation damage in the main solar power plant.

The highest-energy proton detector of the three carried by the satellite measures protons above 50 Mev. The medium-energy detector measures in a well defined energy interval between 26 and 34 Mev. The results for these two detectors are simpler than the electron case because of the relative time stability of the proton distributions that they measure and the simplicity of their detection sensitivity. The spatial distribution of these protons and the energy spectrum that can be derived from them will be discussed in Section 2.3. The remaining half of the damage to the Telstar solar power plant is caused by protons. The fourth detector in the satellite measures low-energy protons between 2.5 and 25 Mev and provides rather detailed information on the spectrum, particularly below 12 Mev. The analysis of these data is not yet complete and the results from this detector are not included in this paper.

The period between July 10, when the Telstar spacecraft was launched, and the end of October, 1962, has been of special interest. This period begins just after the United States high-altitude nuclear test (Starfish)

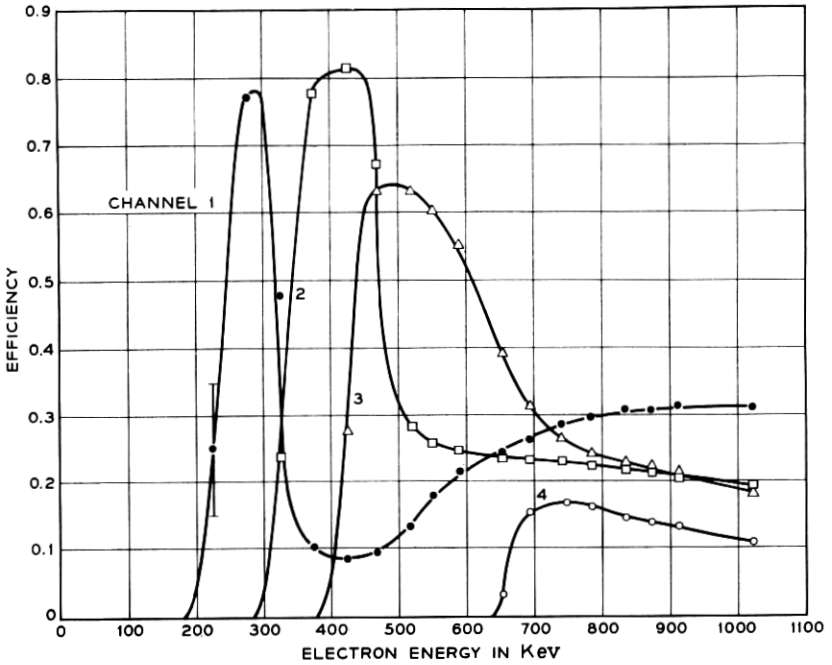

Fig. 1 — Electron detection efficiency as a function of incident electron energy.

of July 9 and ends with the first two Russian high-altitude nuclear tests on October 22 and 28. During most of this time, the Telstar satellite was the only intermediate-altitude radiation monitor in space. In these months, 770 hours of usable telemetry was acquired by the NASA tracking network and the Bell System telemetry stations at Andover, Maine, and Cape Canaveral, Florida. Although some later data are used, it is the 180,000 data points which represent the output of the electron and the two higher-energy proton detectors for the first 104 days in orbit that form the basis of the charged particle distributions that follow.

1.2 *Radiation Damage Experiments*

Radiation damage effects on the bulk properties of silicon are directly observed in the short-circuit current of four solar cells and in the common-base direct current gain of six specially fabricated silicon transistors. The details of these devices and the type of information they provide are described in an accompanying paper.[1] In addition to these special experiments, the main solar power plant provides a large statistical study of damage to several thousand essentially identical devices

measured together. The present paper will describe the results from all three of these sources and will relate the damage observed to the radiation exposure of the satellite as calculated from the particle experiments. Particular attention will be centered on the first 104 days in orbit because the particle distribution has been studied in detail during this time.

II. PARTICLE EXPERIMENTS

2.1 *General*

2.1.1 *Motion of Geomagnetically Trapped Particles*

The basic motion of a charged particle trapped in the earth's magnetic field is a spiral around a magnetic line of force; see Fig. 2. As the

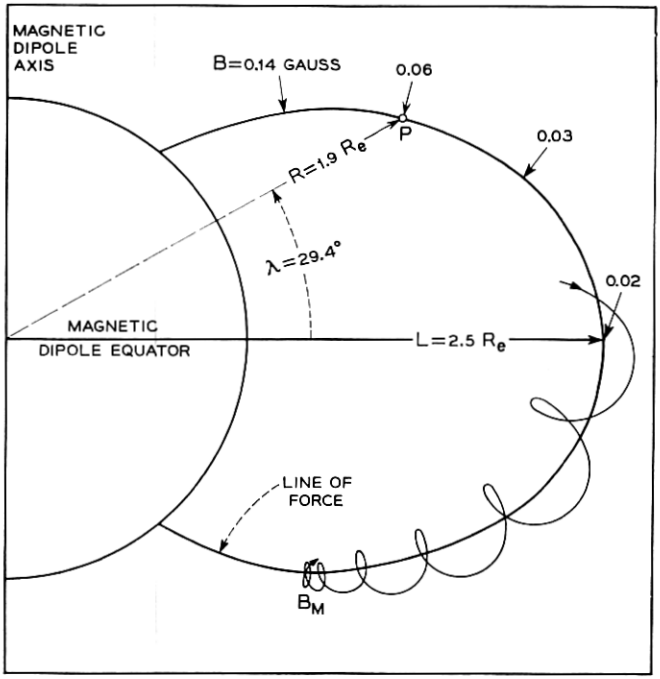

Fig. 2 — The motion of a charged particle trapped in a dipole magnetic field. The particle is confined near the magnetic shell $L = 2.5\ R_e$ and is mirroring at field strength B_m. The B-L coordinates of the point P are $B = 0.06$ gauss and $L = 2.5\ R_e$. The R-λ coordinates of the point P are $R = 1.9\ R_e$ and $\lambda = 29.4°$. Distances are measured in units of earth radii, R_e.

particle gets nearer to the earth and into regions of higher magnetic field strength, the spiral becomes flatter until eventually the particle is reflected and goes back out along the line of force. A given particle is always reflected at the same value of the field strength, B_m (B_{mirror}). The mirror point depends upon the angle between the particle velocity vector and the magnetic field vector at the magnetic equator. Particles moving very nearly parallel to the field line at the equator mirror close to the earth, at large values of B_m, while particles moving nearly perpendicular to the field line at the equator mirror close to the equator, at nearly equatorial values of the field. Superimposed on the back and forth motion in the magnetic field is a small but important longitudinal drift, westward for protons and eastward for electrons. These motions, their stability and various injection and loss mechanisms have been treated in considerable detail in the literature.[2-14] The longitudinal drift shifts the particles so that they spiral about longitudinally adjacent lines of force which are equivalent. The set of equivalent lines of force is called a magnetic shell. Thus, a particle is constrained to move so that the locus of the center of its spiral always lies near the same magnetic shell, and is confined to regions on the shell with magnetic fields equal to or less than B_m. A natural coordinate system in which to consider this motion is one which identifies the magnetic shell appropriate to the particle and then measures position in the shell in terms of the magnetic field strength. Such a coordinate system has been developed and is described below.

2.1.2 *Coordinate Systems*

A transformation developed by McIlwain[15] maps the earth's magnetic field onto a dipole field having the same first moment. In the axially symmetric dipole field, a magnetic shell is defined simply as the surface generated by rotating a line of force about the dipole axis. The magnetic shell is labeled by L, the distance from the dipole axis in the equatorial plane of the dipole. Position in the magnetic shell is given by the field strength, B, Fig. 2. Because of the additional symmetry of the dipole field, a quarter of a meridian plane is a complete representation. The B-L coordinate system is well suited to many theoretical calculations, and we have done most calculations and present some results in this system. However, the geometrical distortions inherent in the transformations make it difficult to get an intuitive picture of the spatial distribution of the particles in B-L coordinates. For this reason, we present many results in the magnetic dipole polar coordinates R and λ,

Fig. 2, which give a pseudo-geographic representation. Both R and L will be measured in units of earth radii, R_e, in what follows. As a result of the anomalies in the real field, the surface of the earth is very wrinkled in R-λ coordinates. Some of the wrinkles exceed 0.1 R_e in extent.

The magnetic field used to calculate the coordinates is a 48-term spherical harmonic expansion with the Jensen and Cain[16] coefficients for 1960. The coordinates are only as good as the expression for the magnetic field, $\pm\approx 2$ per cent.[53] In addition, the magnetic field is assumed to remain fixed, whereas the field in space is known to vary as a result of fluctuations in the earth's magnetization, currents in the ionosphere, currents due to circulating magnetically trapped particles, and other perturbations connected with solar activity. The coordinate system as used here acts as a fixed grid against which changes in both the magnetic field and the particle population are measured. The two effects are not separable, but in the part of the magnetosphere covered by the Telstar satellite the magnetic variations are small compared to the changes in the particle population.

2.1.3 *Treatment of the Data*

The counting rates of the various channels of particle information are deduced from readings of the 14-bit binary register in the telemetry,[17] modified in the case of register overflow in accordance with analog readings of log ratemeters in those channels to which the ratemeter information applies.[1] It is convenient to report the distribution of a particular class of particles in space in terms of its omnidirectional flux, defined as the number of particles passing through a sphere of unit cross-sectional area per unit time. Deducing this quantity requires a knowledge of the efficiency of the detector, which in turn depends on the energy spectrum of the particles being measured. To obtain a number which expresses the data more directly, we have chosen to define an omnidirectional counting rate (OCR) which contains all the geometrical factors required to specify an omnidirectional flux, but which does not contain a factor for the detector efficiency. The efficiency can be specified for an assumed particle spectrum by integration over curves of the type shown in Fig. 1. For example, if the electron spectrum is that corresponding to equilibrium beta decay from fission fragments, channel 3 of the electron detector has an efficiency of 0.2, and a flux can be deduced from its OCR by multiplying by 5. In principle, several parameters of an approximate spectrum and the corresponding detector efficiency can both be deduced by iteration, using the efficiency curves for monoenergetic particles. This process has not yet been carried out in detail.

The angular distribution of particles at any particular point in space is far from isotropic, and the omnidirectional flux (or omnidirectional counting rate) is the average over all directions. The two proton detectors whose results will be described in Section 2.3 are essentially omnidirectional detectors in their construction; that is, they measure an approximately equally weighted average of the proton flux from all directions. The electron detector, however, is highly directional. Its axis is normal to the spin axis of the satellite and hence, over a number of satellite rotations, it measures an average directional intensity that depends on the angle between the satellite spin axis and the local magnetic field. The average directional counting rate has been converted to an omnidirectional counting rate (*OCR*), using an approximate expression for the influence of the aspect of the satellite.

$$OCR = \frac{C/G}{1 + 0.4 \cos 2A}, \tag{1}$$

where C is the average directional counting rate, G is the geometrical factor of the detector, and A is the angle between the spin axis and the local magnetic field. A more exact expression would take into account the anisotropy of the angular distribution of the particles at the particular location at which the measurement is being made and hence would vary from one place to another in space. Expression (1), however, is a good approximation over most of the space investigated. For the omnidirectional proton detectors, the *OCR* involves only the counting rate and the geometrical factor of the detector. Note that the *OCR* has the same units as omnidirectional flux ($1/\text{cm}^2$ sec) throughout the paper. The *OCR* has been written most conveniently in terms of the variable Φ defined by

$$\Phi \equiv \log_{10} (OCR). \tag{2}$$

From a knowledge of the satellite ephemeris and the orientation of the satellite spin axis, the coordinates B-L or R-λ and the angle A are calculated and associated with the *OCR* as defined above. The data have then been machine plotted in a number of different forms:

Plot 1. *Constant* OCR *contours in* R-λ *space.* The plotting coordinates are R and λ. For a given detector, a point is plotted if Φ and the time, T, at which the datum point was taken fall within specified intervals. Fig. 3 is a plot of all the points for which data are available in electron channel 3 between days 263 and 267, 1962. Fig. 4 is a plot of all the points in Fig. 3 for Φ-range 2 (contour 2), Table I. The inner-belt contour stands out clearly. These plots give the flux distributions in space.

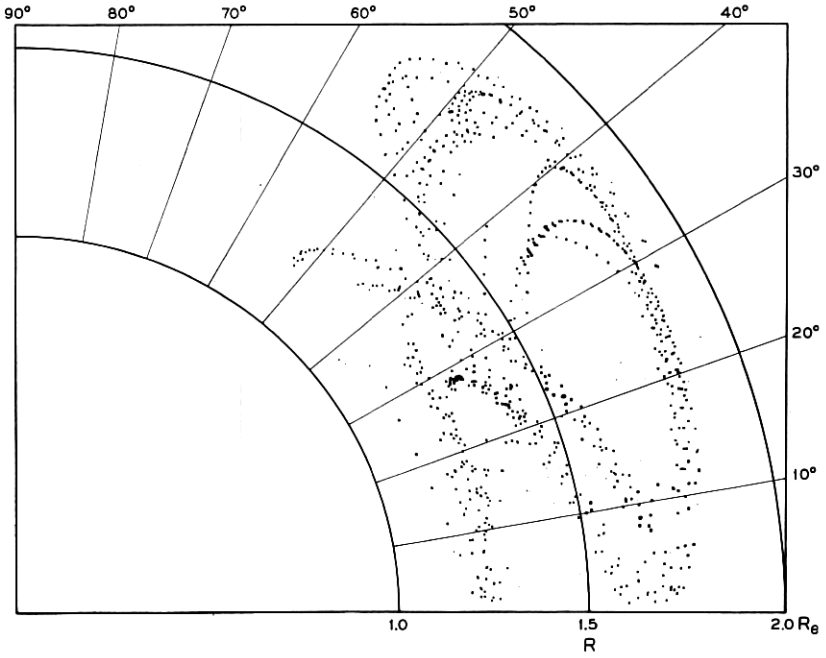

Fig. 3 — Points at which data were acquired in electron channel 3 for days 263 to 267, 1962, plotted in R-λ coordinates. The surface of the earth occurs at $R = 1.0 \pm 0.1\ R_e$.

Plot 2. *Constant* OCR *ratios in* R-λ *space.* These plots are analogous to plot 1, except that a range of $\Phi_a - \Phi_b$, where a and b indicate different channels, is selected instead of a range of Φ_a . These plots give an indication of the energy spectrum.

Plot 3. *Constant* OCR *contours in* B-L *space.* The difference between plots 1 and 3 is that B and L are used as plotting coordinates for plot 3 instead of R and λ. The geometry of the two coordinate systems is very different and they are appropriate to different calculations.

Plot 4. *Constant* OCR *ratios in* B-L *space.* The remarks under plot 3 apply.

Plot 5. Φ *vs* T. Under strict constraints, Φ values separated in time by not more than two minutes are interpolated to find Φ at given values of L. Φ is then plotted against T in days for the given value of L and a small range of B. The resultant plots give a time history of the radiation in almost 200 limited regions of space.

Plot 6. Φ *vs* B. Φ is interpolated to specific values of L, as in plot 5,

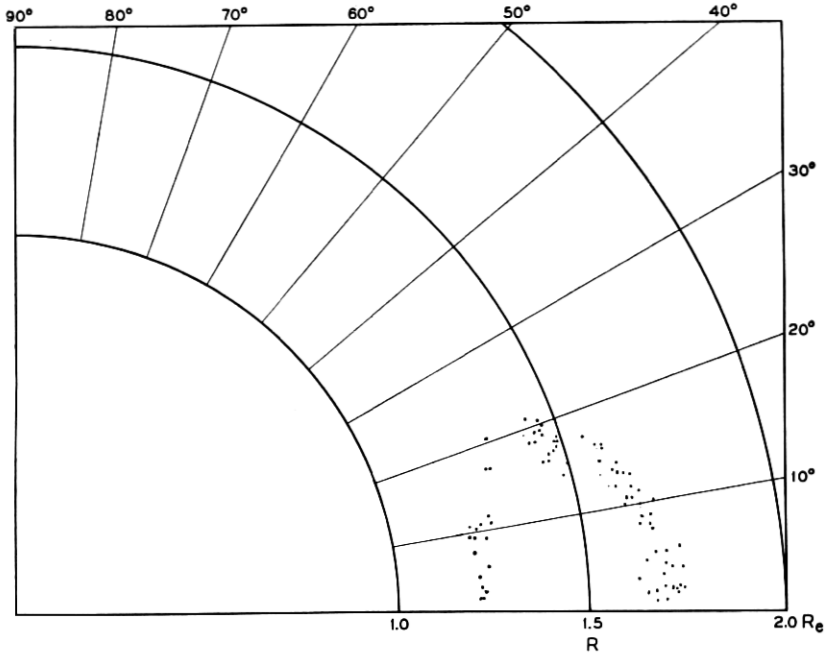

Fig. 4 — Points in Φ-range 2 (contour 2), electron channel 3, days 263 to 267, 1962, plotted in R-λ coordinates. The inner-belt contour is well defined. Φ ranges are defined in Table I.

TABLE I — VALUES FOR THE ELECTRON CONTOURS [OCR has the units counts/cm^2 sec; $\Phi \equiv \log_{10}(OCR)$]

Contour	Φ min	Φ max	Average OCR
1	8.0	≈8.4	1.5×10^8
2	7.5	8.0	6.6×10^7
3	7.0	7.5	2.1×10^7
4	6.5	7.0	6.6×10^6
5	6.0	6.5	2.1×10^6
6	5.5	6.0	6.6×10^5
7	5.0	5.5	2.1×10^5
8	4.5	5.0	6.6×10^4
9	4.0	4.5	2.1×10^4
10	3.5	4.0	6.6×10^3
11	3.0	3.5	2.1×10^3
12	2.5	3.0	6.6×10^2
13	$-\infty$	2.5	$<10^2$

and plotted against B. Only data taken within a given interval of days are included. These plots indicate the distribution of mirror points within a given magnetic shell.

Plot 7. Φ *vs* T. Φ is plotted against T in minutes for each pass. A pass is a single passage within range of a telemetry station. By examining the data in this context, spurious points may be identified. This is most important when the data are sparse.

The material presented in the next section has been selected and synthesized from the seven kinds of cross-referenced plots just described.

2.2 *Results of the Electron Measurements*

2.2.1 *Flux Maps*

Contours of constant *OCR* for electron channel 3 have been drawn through collections of points like those of Fig. 4. Data from the other electron channels have been treated as spectral rather than intensity information. Five of the contour maps thus produced in R-λ space are presented in Figs. 5 through 9. In four cases, the maps cover five-day

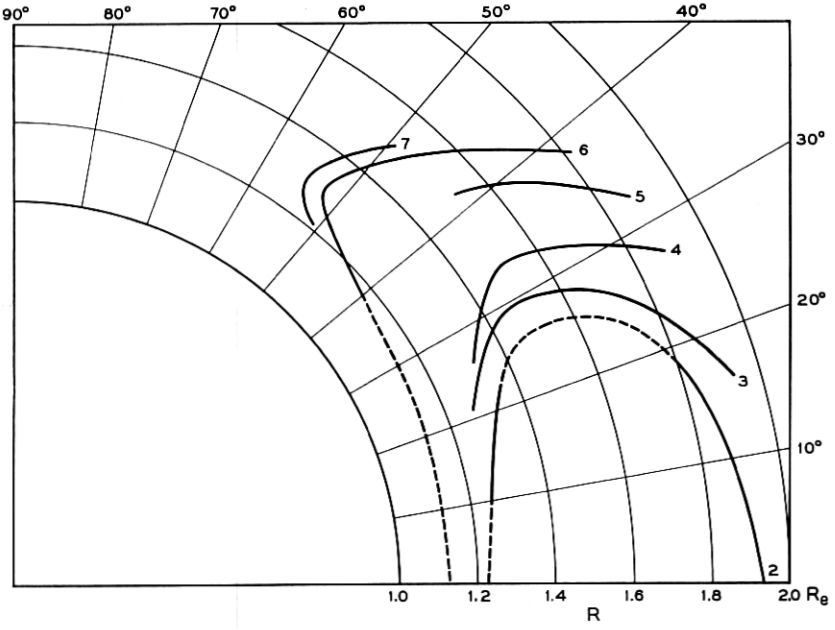

Fig. 5 — Contours of constant *OCR*, electron channel 3, days 193 to 197, 1962, plotted in R-λ coordinates. Dashed lines indicate interpolations and extrapolations. Φ ranges are defined in Table I.

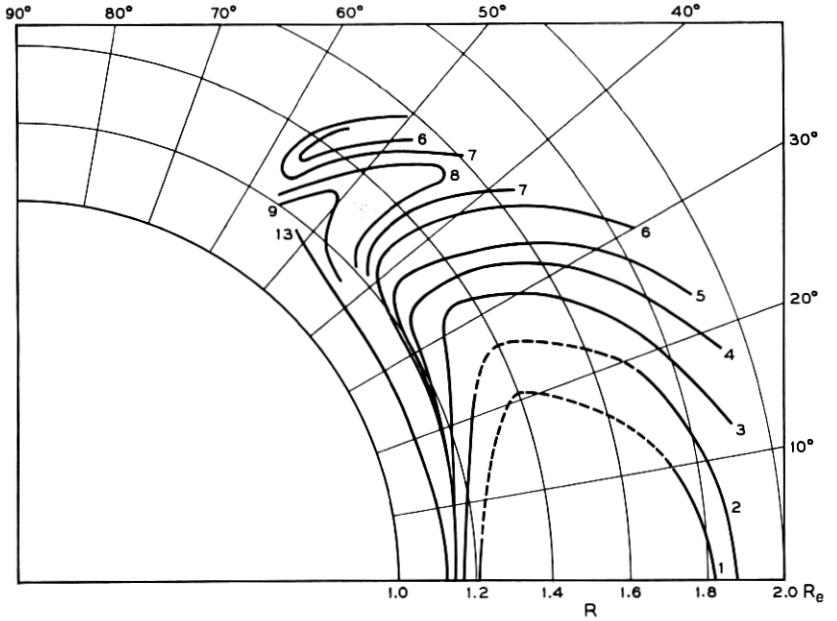

Fig. 6 — Contours of constant *OCR*, electron channel 3, days 203 to 207, 1962, plotted in R-λ coordinates. Dashed lines indicate interpolations and extrapolations. Φ ranges are defined in Table I.

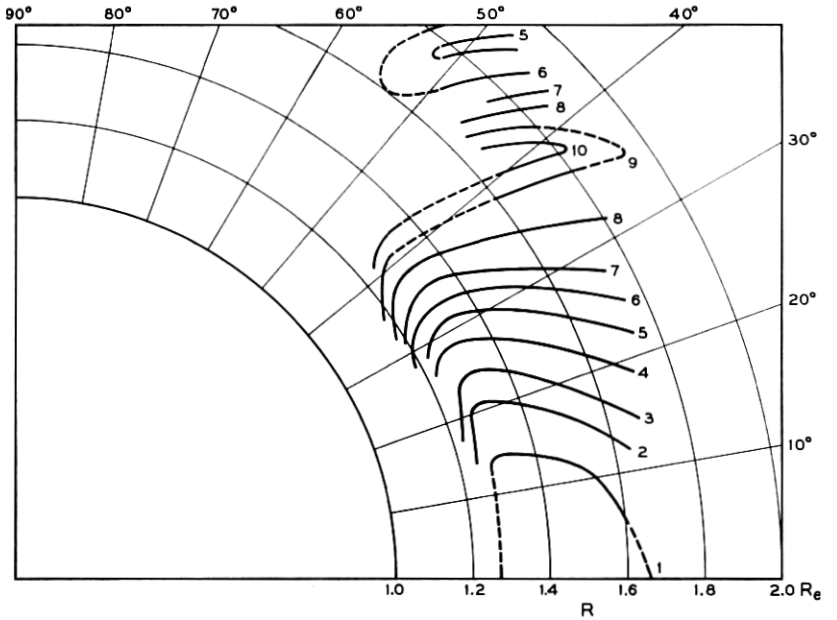

Fig. 7 — Contours of constant *OCR*, electron channel 3, days 238 to 242, 1962, plotted in R-λ coordinates. Dashed lines indicate interpolations and extrapolations. Φ ranges are defined in Table I.

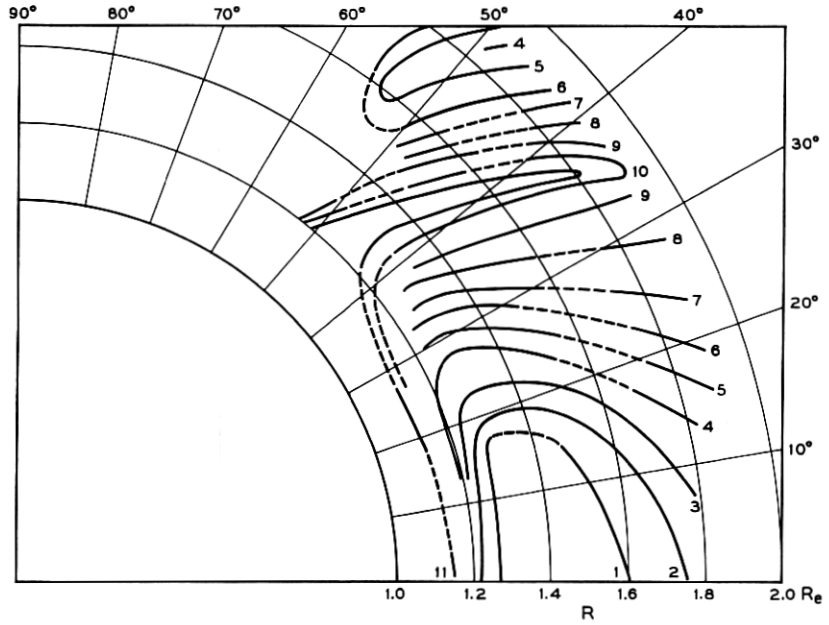

Fig. 8 — Contours of constant *OCR*, electron channel 3, days 263 to 267, 1962, plotted in R-λ coordinates. Dashed lines indicate interpolations and extrapolations. Φ ranges are defined in Table I.

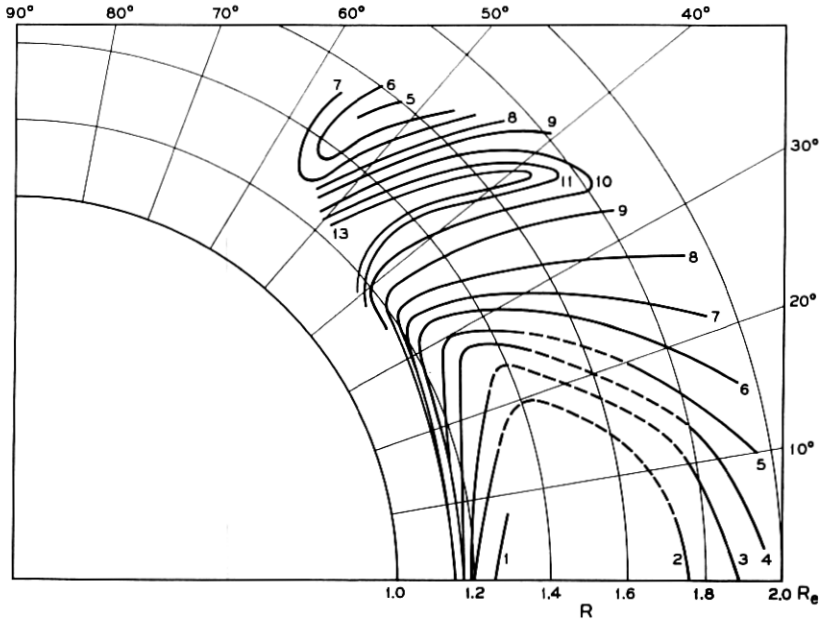

Fig. 9 — Contours of constant *OCR*, electron channel 3, days 288 to 294, 1962, plotted in R-λ coordinates. Dashed lines indicate interpolations and extrapolations. Φ ranges are defined in Table I.

intervals, the earliest containing the data for days 193–197, starting two days after the Telstar launch and three days after the Starfish nuclear test. The latest map, covering the seven-day period, days 288–294, is for the week immediately preceding the first of the Russian high-altitude nuclear tests on October 22. The counting rates of adjacent contours on these plots are separated by $\sqrt{10}$ in *OCR* or by 0.5 in Φ, as indicated in Table I. An exception is contour 1, for which the actual data do not uniformly cover the half decade counting rate range that would be assigned to this contour in the normal progression. A second exception is contour 13, which indicates the limit beyond which the counting rate is not measurably different from 0. The contour maps for each five-day interval have been drawn by hand essentially independent of one another, and there are minor changes in contour shapes and positions which do not represent the optimum contour fitting to the data taken as a whole. A more comprehensive processing of the data is in progress. Dashed lines on the contour maps indicate extensions of the contours into regions devoid of data. Such regions shift with time as the orbit of the satellite precesses, a feature which will be discussed more fully in Section 2.4.1.

The highest electron fluxes lie on the equator in a region centered at a radial distance of about 1.45 R_e. This is the general region of the inner Van Allen belt. The contours lie increasingly close together as one proceeds to lower altitudes from this maximum because of the removal of particles from trapped orbits by the increasingly dense atmosphere. In Figs. 6 through 9 the tip or horn of the outer Van Allen belt is also clearly evident in the secondary maximum at $\lambda \approx 50°$ and $R \approx 1.5\ R_e$. The separation into two belts is not apparent on days 193-197, partly because the orbit stops short of the outer belt maximum, but even more importantly, because the region between the two belts on those early days is filled with electrons, presumably from the Starfish explosion. Through the sequence of five figures a minimum-intensity slot between the inner and outer belts continually develops until on days 288-294 it contains a counting rate immeasurably different from 0 in the Telstar electron detector. During this period, all the contours around the inner belt peak are contracting. This occurs more rapidly on the lower-intensity contours and at larger values of R and λ than in the low-R nearly equatorial region, but nowhere as dramatically as in the region of the slot. This time decay will be discussed in more detail in Section 2.2.3.

Figs. 10 and 11 show contours of constant *OCR* in the *B*-*L* representation, corresponding to the contours in R-λ space shown in Figs. 6 and 9, respectively. The distortions introduced by the *B*-*L* coordinates show

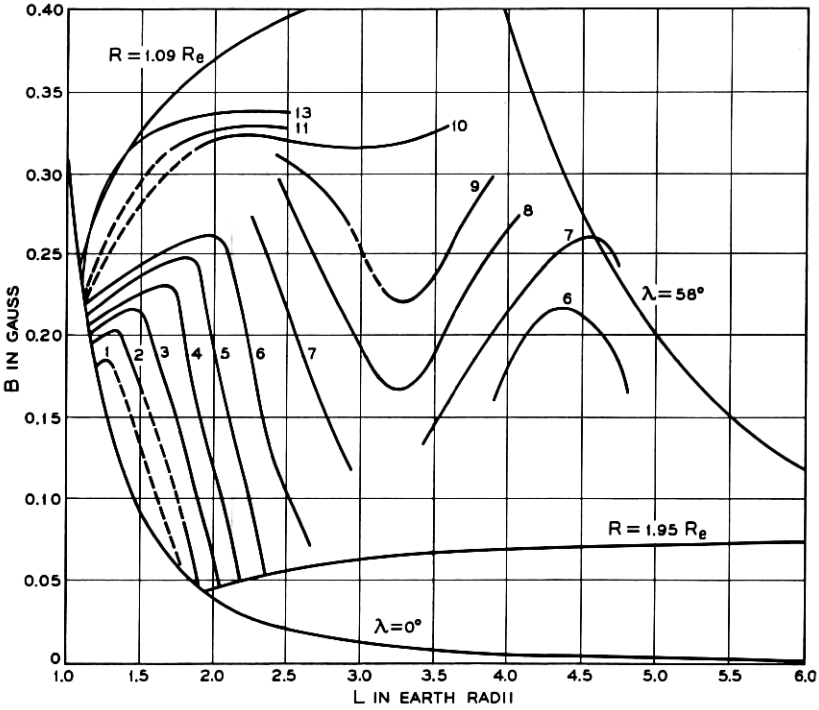

Fig. 10 — Contours of constant *OCR*, electron channel 3, days 203 to 207, 1962, plotted in *B-L* coordinates. Dashed lines indicate extrapolations and interpolations. The lines $R = 1.09\ R_e$, $R = 1.95\ R_e$ and $\lambda = 58°$ define the approximate boundaries of the space swept out by the Telstar orbit. Φ ranges are defined in Table I.

graphically in contour 1 and in the appearance of the horn of the outer belt. The *B-L* diagrams contain three lines that approximately bound the Telstar orbit: $R = 1.09\ R_e$, the lowest altitude limit; $\lambda = 58°$, its extreme in equivalent dipole latitude; and $R = 1.95\ R_e$, the upper altitude extreme. All of the space more distant from the earth than the Telstar satellite can observe is compressed between the $R = 1.95\ R_e$ line and the $\lambda = 0°$ line, the trace of the equatorial plane of the magnetic dipole in this space. The orbital integrals which will be described in Section 2.4 have been conveniently carried out in *B-L* space.

2.2.2 *The Energy Spectrum*

As discussed in Section 1.1, the major sensitivity of the electron detector is to electron energies between 0.25 and 1 Mev. The detector

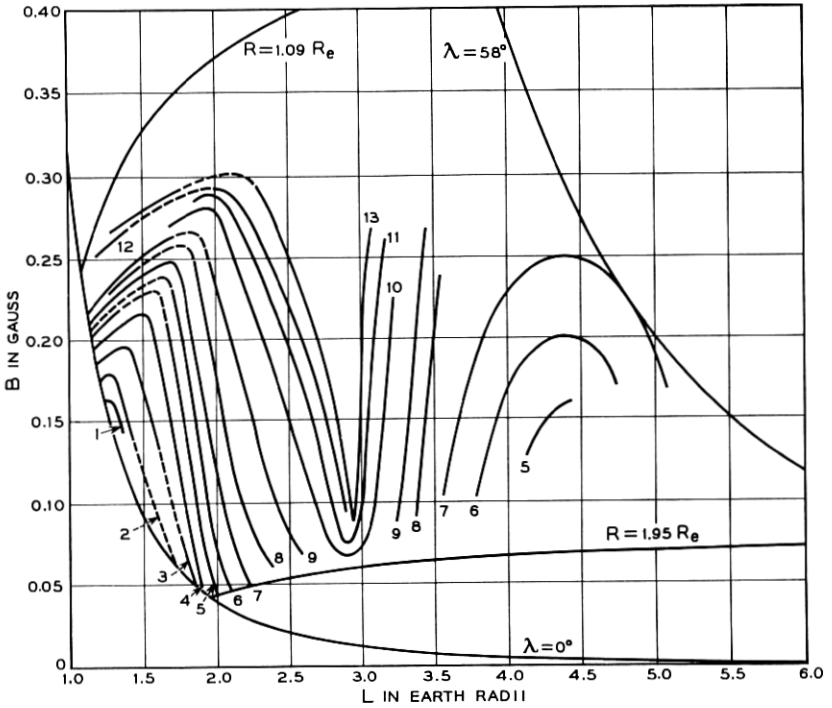

Fig. 11 — Contours of constant *OCR*, electron channel 3, days 288 to 294, 1962, plotted in *B*-*L* coordinates. Dashed lines indicate extrapolations and interpolations. The lines $R = 1.09\ R_e$, $R = 1.95\ R_e$, and $\lambda = 58°$ define the approximate boundaries of the space swept out by the Telstar orbit. Φ ranges are defined in Table I.

gives only an indirect indication of the spectrum above 1 Mev, an energy region which contributes heavily to radiation effects. The ratios, ρ_{34}, of channels 3 to 4 for two five-day periods are indicated in Figs. 12 and 13. Unfortunately, channel 4 has no log ratemeter and ratios cannot be taken in the high-intensity region inside contour 3, where the register begins to overflow. During mid-July, ρ_{34} had a value of approximately 3 over much of the space accessible to the instruments. This is exemplified by the region marked C in Fig. 12. A ratio of 3 is consistent with an electron spectrum appropriate to fission fragment beta decay.[18,19] Such consistency does not, however, constitute a unique determination of such a spectrum. Without postulating an extremely complex spectrum with a maximum intensity at about 700 Kev, a ρ_{34} equal to 3 cannot be produced unless there is a significant population of electrons in excess of 1 Mev. It is not possible, however, to assert that the fraction of electrons

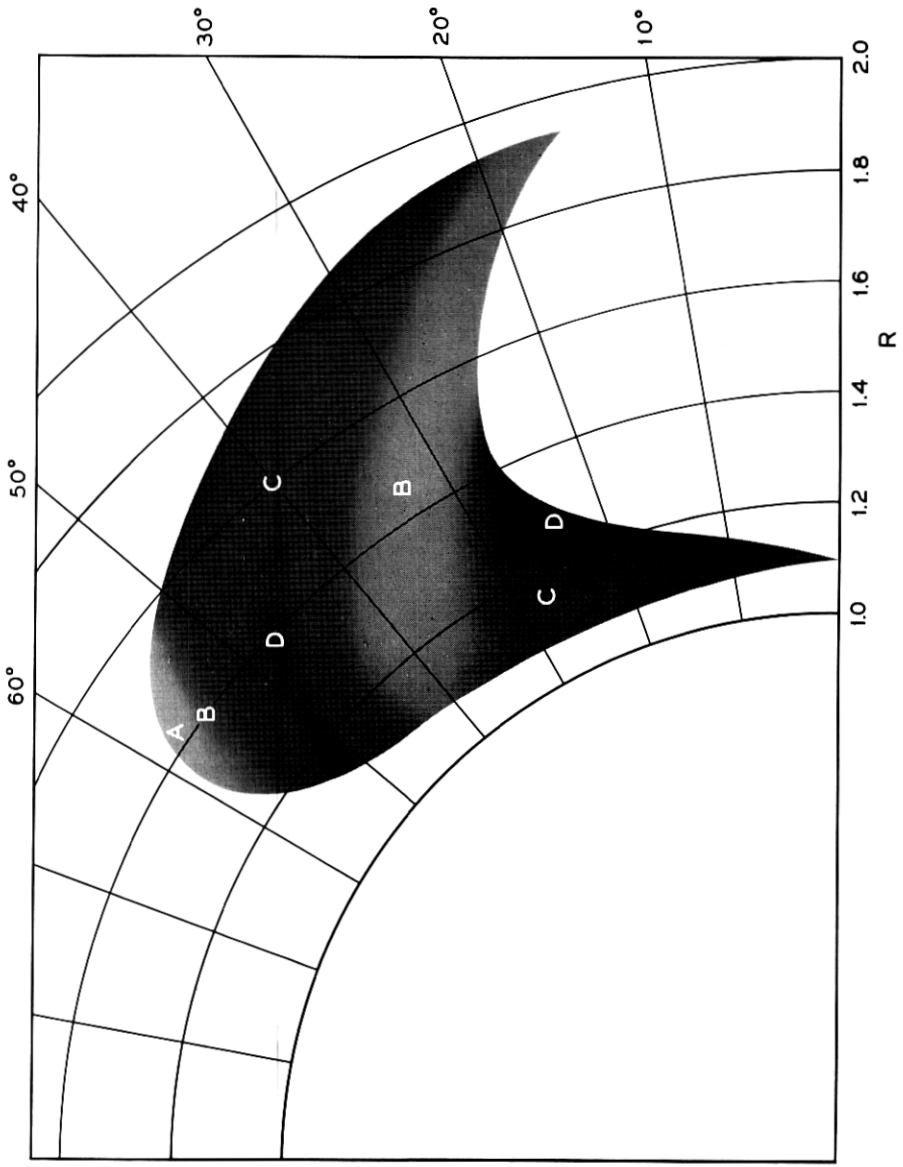

Fig. 12 — Ratio of *OCR* electron channel 3 to *OCR* electron channel 4 (ρ_{34}), days 203 to 207, 1962, displayed in R-λ coordinates.

Label	Range of ρ_{34}	Comment
A	>8	very soft
B	4–8	soft
C	2–4	fission-like
D	1–2	hard

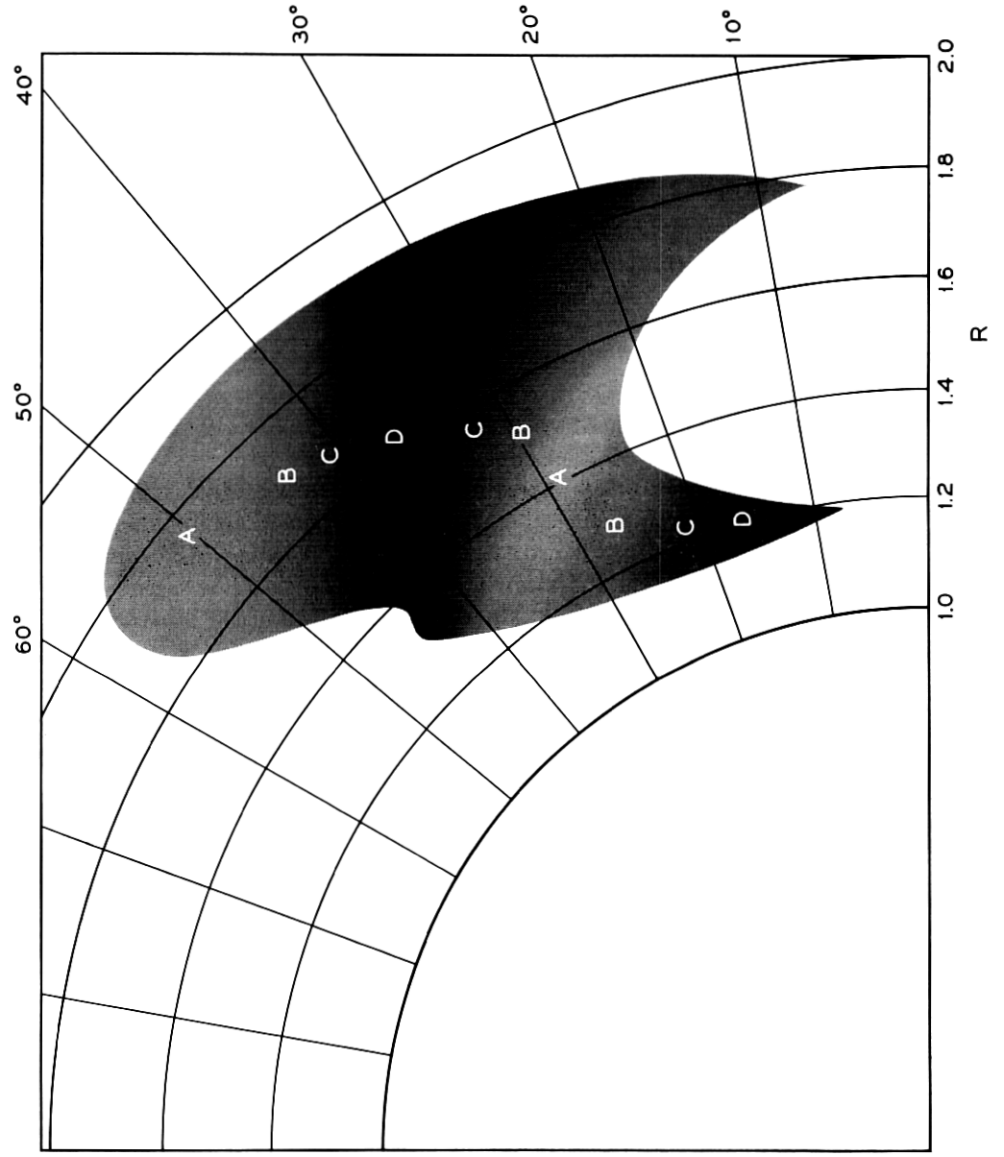

Fig. 13 — Ratio of *OCR* electron channel 3 to *OCR* electron channel 4 (ρ_{34}), days 263 to 267, 1962, displayed in R-λ coordinates. Labels are identified in the legend of Fig. 12.

above about 1.5 Mev is 0.2 of the total electron spectrum, as would be the case in the fission spectrum.[19]

Van Allen, Frank, and O'Brien[20] have reported on measurements from an instrument in the Injun I satellite that effectively measures electrons above 1.5 Mev.[21] They have concluded that the spatial distribution of the energetic electrons injected by Starfish had a maximum at $L \approx 1.2$ R_e, and they have inferred that the flux is 10 per cent of this maximum at an equatorial L of about 1.8 R_e. From the Telstar data shown in Fig. 6, the electron flux at $L = 1.8$ R_e on the equator is essentially the same as that at $L = 1.2$ R_e, and contour 3, which is 10 per cent of the maximum measured value, apparently has an upper crossing of the equator at $L \approx 2.1$ R_e. When these two sets of observations are translated into R-λ space, they give high-intensity regions very different in extent and will, if one asserts that the electrons seen by the Telstar detector are a result of Starfish, give rise to quite different values of the total number of electrons injected into trapped orbits by that explosion. Since the two detectors measure electrons at quite different energies, the apparent conflict between these two sets of results is easily resolved by proper treatment of the electron energy spectrum. The higher flux of electrons for $L > 1.6$ R_e as seen by the Telstar detector do not have associated with them the proportion of high-energy electrons to be expected in a fission electron spectrum. The possibility has been considered that most of the lower-energy electrons (the Telstar data) on these higher-L lines may be of natural origin. However, the time-dependence of the measured flux, which will be discussed in Section 2.2.3, strongly suggests that a major fraction of these electrons was connected with the explosion. A mechanism is thus required by which a high-altitude explosion can introduce a spectrum of electrons which varies in space and can be appreciably different from that of fission beta decay. Although the details of such a process are not yet understood,[22] direct observation of this effect on a less extensive scale was made by Explorer XV[23,24] on electrons injected by the second Russian high-altitude explosion on October 28. Several mechanisms for degrading the electron energy spectrum from a fission electron source have been suggested.[25,26] It also seems possible that low-energy electrons (<0.25 Mev) normally present in space might be accelerated as a result of the shock front of the expanding bomb debris to energies where they would be counted by the Telstar electron detector. A quantitative determination of the spatial variation in the electron spectrum which will satisfy the July measurements of the Telstar and Injun satellites has not yet been made, but with recognition of a softer spectrum on higher-L lines there seems

little doubt that a large part of all the electrons measured by the Telstar satellite in July were a result of the Starfish test.

In the tip of the outer belt, region A of Fig. 12, the spectrum softens appreciably, $\rho_{34} > 8$, and a similar but less pronounced softening occurs in region B. In the small regions D, the spectrum was apparently harder, $2 > \rho_{34} > 1$, than a fission beta spectrum. It is very difficult to see how a ratio smaller than 2 can be obtained for any electron spectrum in the light of the efficiency curves of Fig. 1, and the low ratios seem to arise from two other effects. In the lower-intensity of the two regions marked D (at high λ), ratios of <2 arise from statistical fluctuations in the number of counts in the register. In the high-intensity D region, these anomalous ratios arise from fluctuations in the log ratemeter measurement of the counting rate of channel 3, which is modulated as the spin of the satellite sweeps the acceptance cone of the detector through the nonisotropic particle distribution.

The temporal changes in the electron belts are heavily energy dependent. By late September, Fig. 13, the configuration is still fissionlike, as indicated by ρ_{34} only in the areas marked C. The spectrum is soft on the high-altitude slope of the inner belt, very hard in the slot, and soft again in the tip of the outer belt. The higher-energy electrons appear (surprisingly) to decay faster on the high-altitude slope of the inner zone, while the lower-energy electrons seem to disappear more rapidly in the center of the slot, at $L = 3\ R_e$.

Until about September 23, the ratio, ρ_{13}, of channel 1 to channel 3 on the Telstar detector indicates that between 0.25 and 0.6 Mev the spectrum is very soft, $\rho_{13} > 8$, in the slot and contains appreciably more low-energy electrons than a fission beta-decay spectrum except at very low altitudes and the center of the inner belt. Beginning on September 23, there is a very extensive and complex change in the electron population for $L > 1.8\ R_e$ and particularly for lower-energy electrons. The changes are small in channels 3 and 4, but are sufficiently large in channels 1 and 2 to have a profound influence on the ρ_{13} ratio in some places. These effects are apparently of natural origin. They have not yet been studied in sufficient detail to permit discussion in this paper.

2.2.3 *Time Variation*

The time variation of the electron flux will be discussed in terms of the omnidirectional counting rates of channel 3. The other channels show generally similar time decays, but there are differences in detail which give rise to the changes in the spectrum discussed above. Figs. 14

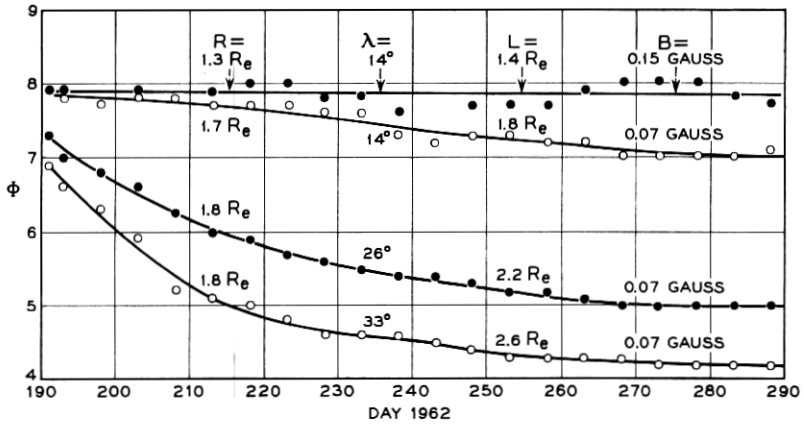

Fig. 14 — Temporal behavior of Φ for electron channel 3 at various positions in the radiation belts.

and 15 have been constructed from type 5 and 6 plots and show the long-term time dependence in representative regions of the belts.

The *OCR* in the high-intensity zone of the inner belt, typified by the point $L = 1.4\ R_e$ and $B = 0.15$ gauss ($R = 1.3\ R_e$, $\lambda = 14°$), shows no net long-term variation. There is some scatter in the points which may be real but which seems more likely to be a result of systematic differences introduced by the interpolations required to remove the B, L, and A dependence of the data. At $L = 1.8\ R_e$ and $B = 0.07$ gauss ($R = 1.7\ R_e$, $\lambda = 14°$) the *OCR* has decayed by somewhat less than a factor of 10 between July and the middle of October, and the rate of

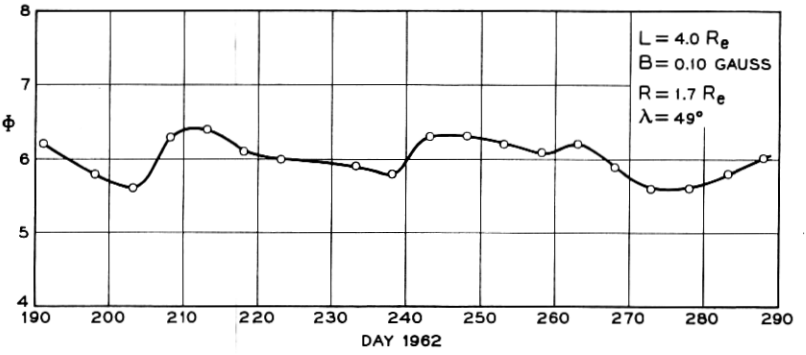

Fig. 15 — Typical temporal behavior of Φ for electron channel 3 in the tip of the outer belt.

decay seems to be slowing. Closer to the center of the slot $B = 0.07$ gauss and $L = 2.2$ and 2.6 R_e ($R \approx 1.8$ R_e and $\lambda = 26°$ and 33°) the decay is faster and greater, and the *OCR* levels off after day 260 at a value 50 times less than it had in early July. The outer-belt horn is characterized by the fluctuations apparent in Fig. 15, at $L = 4.0$ R_e, $B = 0.10$ gauss ($R = 1.7$ R_e and $\lambda = 49°$). The short-term fluctuations are much sharper than those shown in Fig. 15, which have been smoothed over five-day intervals. There is no doubt that the variations here are real, but in these data there appears to be no trend.

In the region below $L = 1.4$ R_e there is general agreement that the bulk of the electrons present were injected by Starfish. This was directly observed as a sudden change by Injun I[20] and TRAAC,[27] both of which had a record of the high-energy electron distribution in this region for many months prior to July. Furthermore, Telstar and Injun measurements in this region have subsequently been verified by other satellites — Explorer XIV,[21] Explorer XV,[23,24] and several Air Force satellites[28-31] — that show the spectra in this region are far too hard to be of natural origin. Since the Telstar satellite was launched a day after Starfish, such a direct statement cannot be made for near equatorial regions with $L > 1.4$ R_e. However, the observation of continuous monotonic decay over the months from July to October, and verification of the absolute intensities observed by the Telstar satellite with measurements by Explorer XV, make it almost impossible to conclude that electrons beyond $L = 1.4$ R_e were not also a result of that test. Electrons were introduced by Starfish even as far out as $L = 3.5$ or 4 R_e. If one adds up the electrons in space as shown on days 203-207, and if the detector efficiency of channel 3 were unity above the threshold, approximately 1.2×10^{25} electrons must have been introduced with energies above 440 Kev. Using the average efficiency (0.38) between 440 Kev and 1 Mev as shown in Fig. 1, the data require at least 3×10^{25} electrons with energies between 440 Kev and 1 Mev. If one uses an efficiency for a fission electron spectrum of 0.2, the number of electrons of all energies was 6×10^{25}. This is something like 10 per cent of all the fission electrons produced in the explosion, although some nonfission source associated with the bomb cannot yet be ruled out.

Fig. 16 presents some preliminary results of observations made during the Russian high-altitude test series. The first two tests, days 295 and 301, injected electrons into the slot region between L values of about 1.8 and 4.0 R_e. After the initial surge we again observe a rapid decay near the center of the slot, and a slow decay near the slopes of the inner and outer belts.

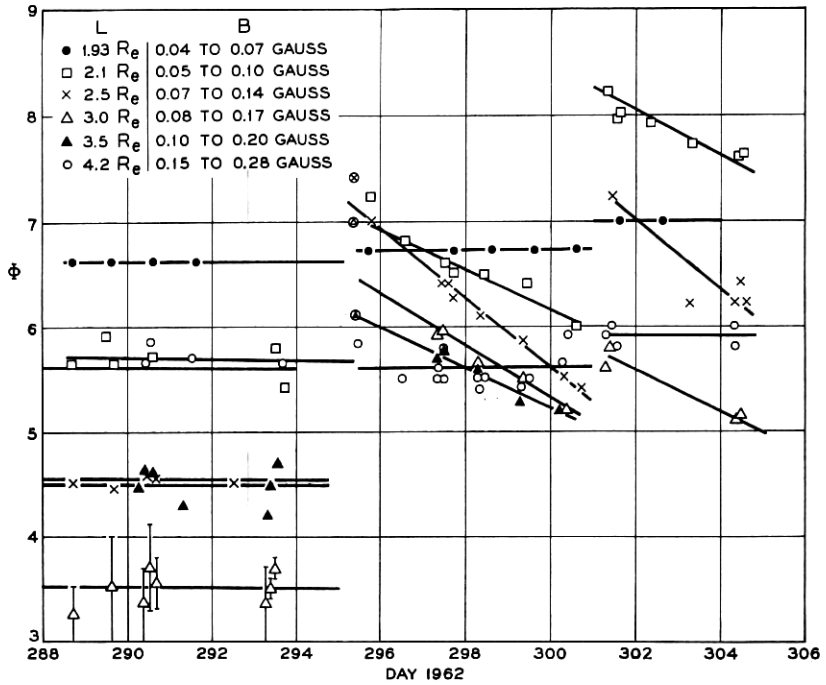

Fig. 16 — Temporal behavior of Φ for electron channel 3 during the first two Russian high-altitude nuclear tests. Circled points on day 295 are probably initial transients.

2.3 *Results of the Proton Measurements*

The *OCR* of the omnidirectional proton detectors have proven very stable in time. This stability has greatly simplified the analysis of the results. Figs. 17 and 18 are maps of the *OCR*, which apply to the entire 15-week period covered. There are five contours per decade in the proton plots, rather than two as in the electron maps previously described. No shift of as much as half a contour (25 per cent) has been observed. The measurements agree well with previous measurements in the inner zone,[32,33] and it seems unlikely that the Starfish test had any appreciable effect on protons in these energy ranges. The maximum intensity occurs at a lower altitude for the higher-energy protons in agreement with theory[10] and other observations.[23,24,34] Both detectors exhibit a well-defined cutoff, beyond which no counts are recorded in the region accessible to the spacecraft. The efficiency of the detectors is high, and

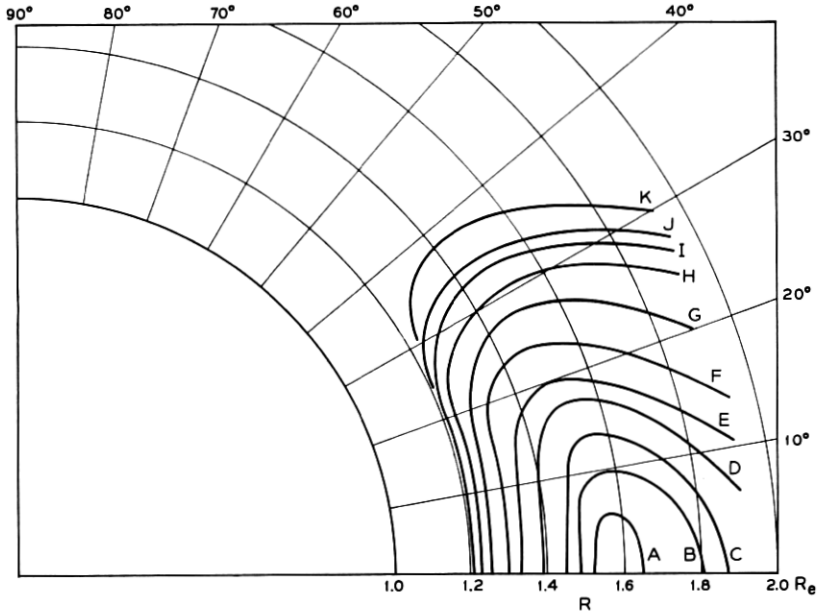

Fig. 17 — Contours of constant *OCR*, protons in the energy range 26 to 34 Mev, days 191 to 294, 1962, plotted in R-λ coordinates. To convert *OCR* to omnidirectional flux (1/cm² sec), add 0.32 to Φ. The range of Φ associated with the contours is: A, 4.0-4.2; B, 3.8-4.0; C, 3.6-3.8; D, 3.4-3.6; E, 3.2-3.4; F, 3.0-3.2; G, 2.8-3.0; H, 2.6-2.8; I, 2.4-2.6; J, 2.2-2.4; K, 2.0-2.2.

using the average efficiency in their regions of sensitivity, the flux is approximately 2.1 *OCR* for the 26 to 34 Mev detector, and 2.6 *OCR* for the >50 Mev detector.

2.3.2 *Energy Spectrum*

The contours for the two detectors have different shapes, which show that the energy spectrum in this range of energies is not constant with position. This is clearly indicated in the equatorial flux plot of Fig. 19. The equatorial omnidirectional *fluxes* for the two detectors are graphed as a function of L. (On the dipole equator $L = R$.) Plotted in the same figure are the quantities N_{26} and n from the expression for the differential spectrum

$$N(E) = N_{26}(E/E_0)^{-n}, \tag{3}$$

where $N(E)$ is the flux of electrons in the energy range dE at E, and

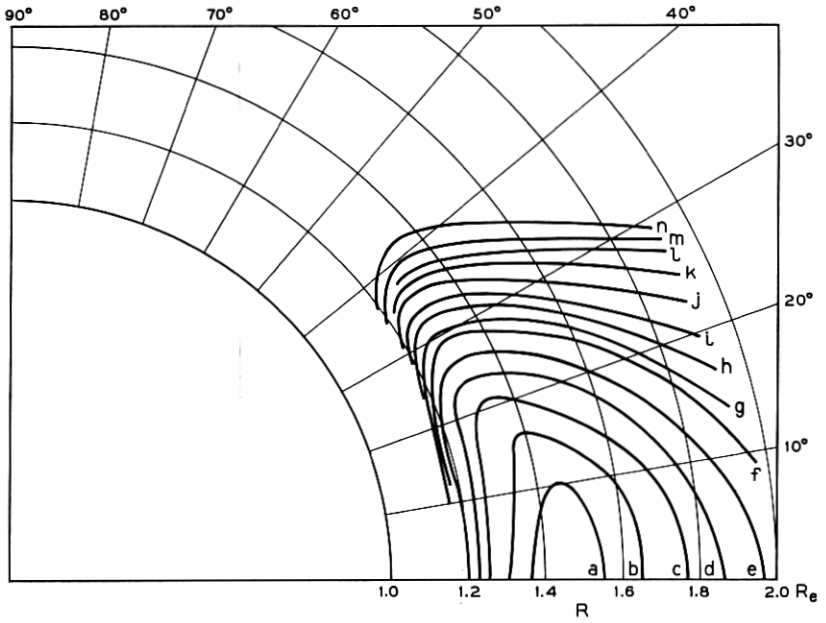

Fig. 18 — Contours of contant *OCR*, protons with energies >50 Mev, days 191 to 294, 1962, plotted in R-λ coordinates. To convert *OCR* to omnidirectional flux (1/cm² sec), add 0.42 to Φ. The range of Φ associated with the contours is: a, 3.2-3.4; b, 3.0-3.2; c, 2.8-3.0; d, 2.6-2.8; e, 2.4-2.6; f, 2.2-2.4; g, 2.0-2.2; h, 1.8-2.0; i, 1.6-1.8; j, 1.4-1.6; k, 1.2-1.4; l, 1.0-1.2; m, 0.8-1.0; n, 0.4-0.6.

$E_0 = 26$ Mev. A fit to the data could have been made with an exponential spectrum of the form[33]

$$N(E) = N_0 \exp(-E/E_c), \tag{4}$$

where N_0 and E_c are constants. However, such a spectrum extrapolates in a very unreasonable way to lower energies, giving far fewer low-energy protons than observed either by the Telstar low-energy proton detector or by detectors on Explorer XV.[24]

With the power law spectrum the value of $n \approx 4.5$ applies over a considerable part of the region beyond the 50-Mev proton maximum, but at smaller L values the spectrum is very much harder and n decreases to a value of about 2. Such a power law variation at low equatorial altitudes seems to be in reasonable agreement with the observations of Freden and White[35] and Naugle and Kniffen.[36]

Using the constants of the spectra as given in Fig. 19, the maximum integral flux of protons with energies >40 Mev is found to be approxi-

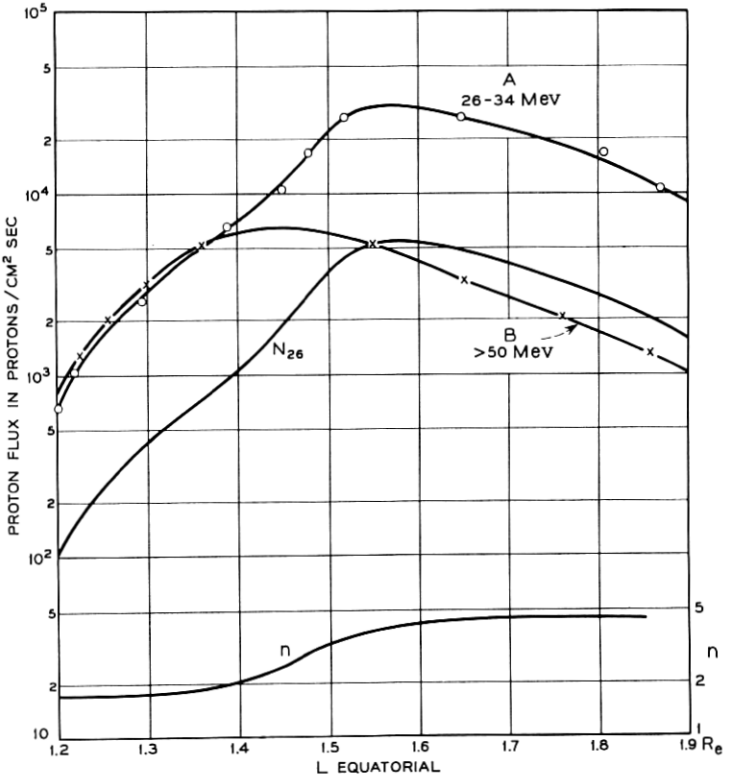

Fig. 19 — Equatorial proton flux. Curve A is for protons in the energy range 26 to 34 Mev, and curve B for protons with energies >50 Mev. n and N_{26} are defined in the text.

mately 1.5×10^4 protons/cm^2 sec, quite close to the historical value of 2×10^4 quoted by Van Allen in 1958[32] for the peak flux in the inner belt.

2.4 *Radiation Exposure of the Satellite*

2.4.1 *Orbital Effects and Method of Calculation*

The radiation exposure of a satellite is an integral along the satellite orbit of the particle flux weighted in accordance with its energy spectrum. The Telstar satellite spends a considerable part of its time in the inner Van Allen belt and thus experiences an unusually rigorous radiation environment. The radiation exposure is far from constant in time, however. The instantaneous exposure varies enormously as the

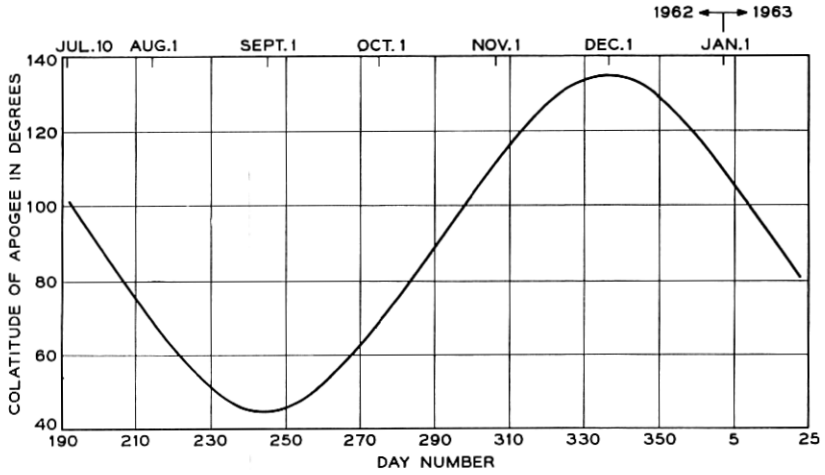

Fig. 20 — The position of apogee colatitude for the Telstar satellite as a function of time.

satellite enters and leaves the region of high intensity in the inner belt. Furthermore, the average exposure over an orbit varies throughout a day because of the geographical asymmetry of the magnetic field that controls the trapped particle distribution. And finally, the average exposure over a period of several days varies as the position of apogee in the orbit precesses. This latter orbital change is shown in Fig. 20, which is a plot of the colatitude of apogee, θ_A, of the Telstar orbit as a function of time. The period of this precession is 181 days, and the maximum and minimum colatitudes are 45 and 135 degrees, corresponding to the 45-degree inclination of the orbit.

To illustrate the wide differences between orbits on a single day, orbits 1 and 6 for day 205 are shown in Fig. 21 in the R-λ space used in displaying the electron and proton distributions. The particles by definition have north-south symmetry in this equivalent dipole representation, but the northern and southern parts of the satellite orbit are far from the same. The differences between the two orbits of the figure near $\lambda = \pm 45°$ are caused primarily by the 11-degree offset of the earth's geomagnetic axis. Near $\lambda = 0°$ and especially at low altitudes, the differences arise from the Brazilian magnetic anomaly. On day 205 of Fig. 21, apogee is near the equator, $\theta_A = 81°$. In contrast, two orbits for day 335, when apogee is at its most southern point, $\theta_A = 135°$, are shown in Fig. 22. These orbital variations from week to week were

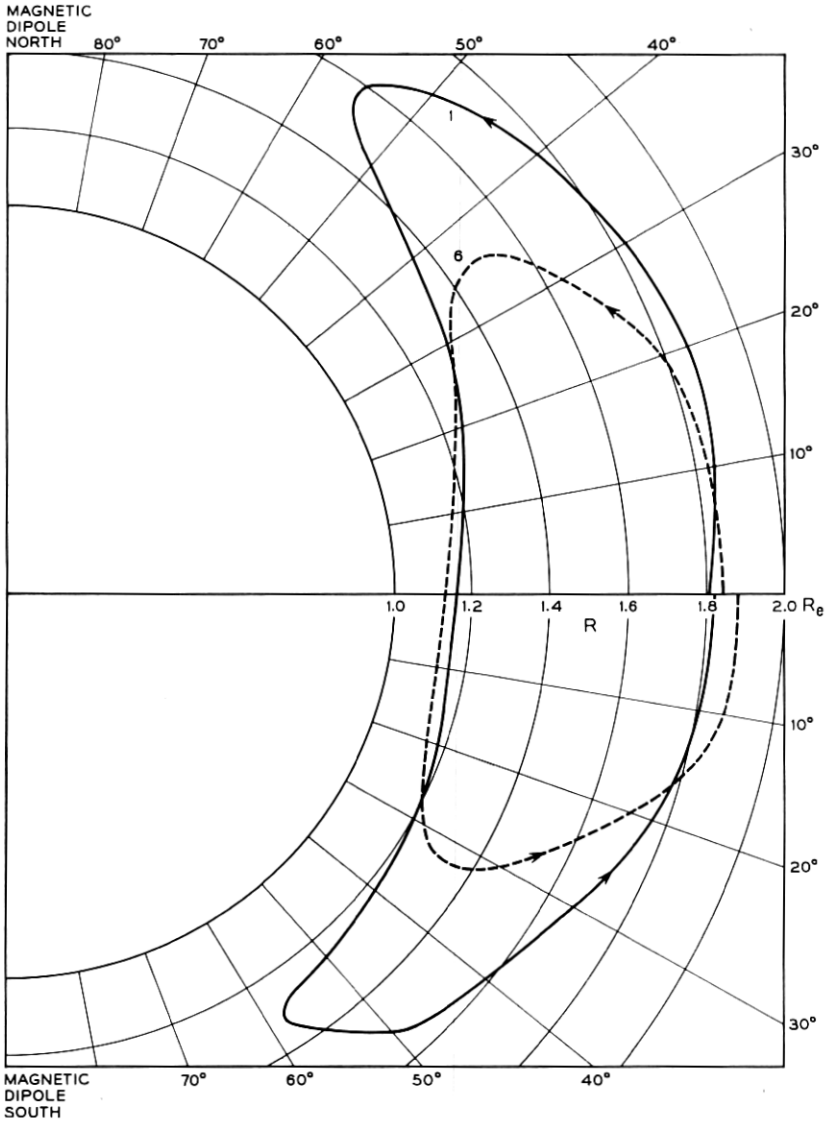

Fig. 21 — Orbits 1 and 6 for day 205, 1962, plotted in R-λ coordinates. Apogee is near the geographic equator.

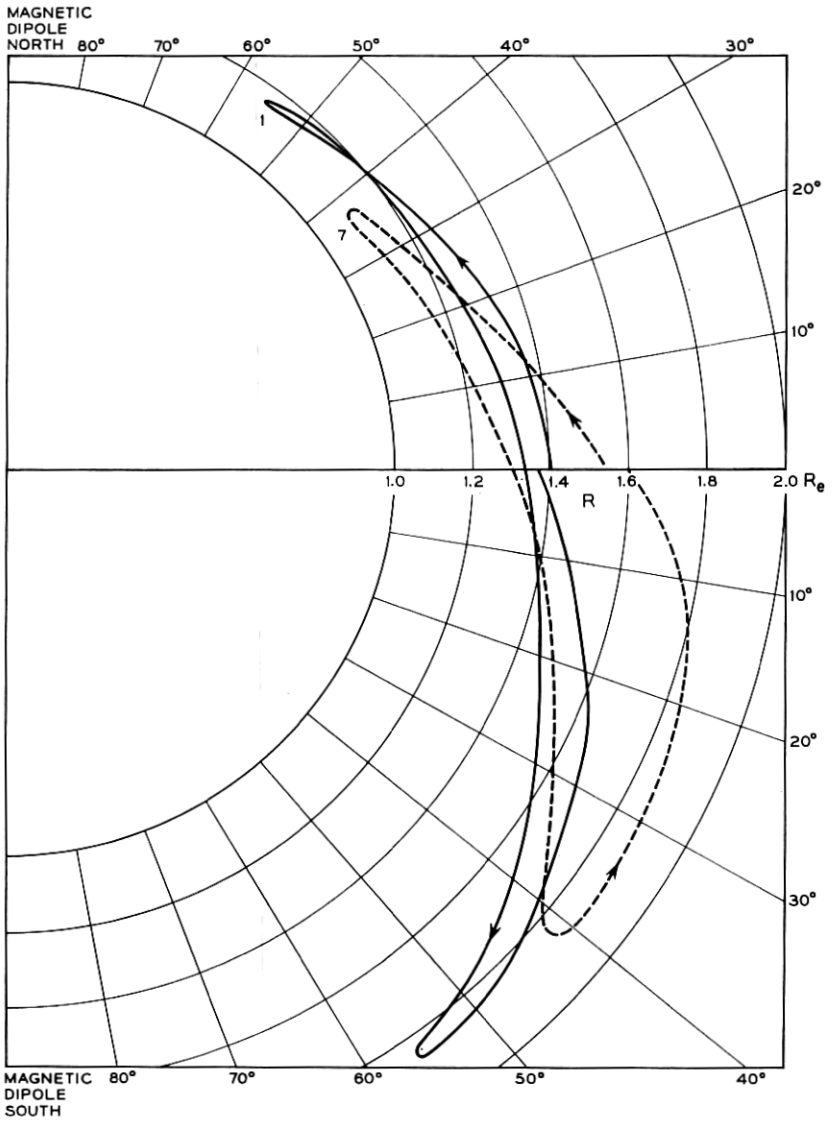

Fig. 22 — Orbits 1 and 7 for day 335, 1962, plotted in R-λ coordinates. Geographically, apogee is at the most southern point in the orbit.

previously noted in connection with regions in B-L space for which data are missing; see Figs. 5-9. The orbital picture is further complicated in computing an integral radiation exposure by the variation in satellite speed along the orbital path, a factor not shown in Figs.

21 and 22. The vehicle spends much more time close to apogee than to perigee. The complex motion of the satellite with respect to the trapped particles makes it necessary to undertake fairly detailed calculations, including transformations to a magnetic coordinate system, in order to find the integrated radiation exposure of the satellite.

The following method has been used. The part of B-L space to which the Telstar satellite is confined has been divided into 620 areas by a grid that is spaced so that the areas are small in the important regions. Thirteen colatitudes of apogee, at 7.5-day intervals, have been selected. For each position of apogee, eighteen equally spaced ascending-node longitudes have been chosen. The fraction of time, T_{ik}, spent in each B-L box has been computed and averaged over the eighteen nodal positions associated with each apogee position, using a Keplerian orbit very close to the Telstar orbit. The step size along the orbit is varied so that the computation is done most accurately in the most critical places. The results of the calculation for $\theta_A = 79.48°$ are shown in Table II. By examining the OCR maps in B-L space, values, OCR_{ik}, appropriate to the days when θ_A had a given value are assigned to the B-L boxes. When necessary a similar procedure is followed for the spectrum, S_{ik}. The operation

$$F = \sum_{i,k} T_{ik} OCR_{ik} S_{ik} \tag{5}$$

is performed. F is now approximately the average flux of all electrons incident on the spacecraft during a one-day period. The calculation is approximate in the sense that the actual orbit, with its continuously varying apogee colatitude and with ascending node longitudes that do not shift by a simple fraction of 360°, has been replaced by a set of closely spaced but discrete orbits. One does not calculate in this way an instantaneous radiation intensity but only an intensity that is very nearly correct over a period of a day or several days. Actually, a more serious inaccuracy is contributed by a lack of detailed knowledge of the particle energy spectrum. This will be described in more detail in connection with specific applications in Sections 3.2 and 3.3.

2.4.2 *Integrated Electron Flux*

Using the method outlined above, the average and cumulative omnidirectional electron flux to which the Telstar spacecraft was exposed have been calculated. The electron flux is obtained from the OCR contours for channel 3 of the electron detector, e.g., those shown in Figs. 10 and 11. These counting rates are multiplied by a factor of 5 to yield the total flux (above 0 energy) under the assumption that the

TABLE II — AVERAGE TIME SPENT BY THE *TELSTAR* SATELLITE IN VARIOUS B-L REGIONS FOR AN APOGEE COLATITUDE OF 79.48°

B_{MIN} gauss	.04	.06	.08	.10	.12	.13	.14	.15	.16	.17	.18	.19	.20	.22	.24	.26	.28	.32	.36	.40
B_{MAX} gauss	.06	.08	.10	.12	.13	.14	.15	.16	.17	.18	.19	.20	.22	.24	.26	.28	.32	.36	.40	.50
L_{MIN} R_e	L_{MAX} R_e	(Entries are in 0.1 Per cent)																		
1.00	1.05	0	0	0	0	0	0	0	0	0	0	0	0	0	0	0	0	0	0	0
1.05	1.10	0	0	0	0	0	0	0	0	0	0	0	0	0	1	2	0	0	0	0
1.10	1.15	0	0	0	0	0	0	0	0	0	0	0	0	6	9	3	1	0	0	0
1.15	1.20	0	0	0	0	0	0	0	0	0	0	2	3	13	4	1	2	1	0	0
1.20	1.25	0	0	0	0	0	0	0	0	1	3	5	3	7	3	1	1	1	0	0
1.25	1.30	0	0	0	0	0	0	0	0	1	1	1	4	4	2	1	0	2	0	0
1.30	1.35	0	0	0	0	0	0	0	0	1	1	0	3	5	2	0	1	1	0	0
1.35	1.40	0	0	0	0	0	0	0	0	1	0	0	3	2	2	1	1	1	0	0
1.40	1.45	0	0	0	0	0	0	0	0	1	0	0	3	4	2	0	0	2	1	0
1.45	1.50	0	0	0	0	0	0	0	0	1	0	1	2	4	2	0	0	1	0	0
1.50	1.60	0	0	0	0	0	0	0	0	1	0	3	3	2	3	1	1	2	1	0
1.60	1.70	0	0	0	0	0	0	0	1	1	1	2	1	6	2	2	0	1	2	0
1.70	1.80	0	7	0	0	0	0	0	2	1	1	3	3	2	2	0	2	1	0	0
1.80	1.90	102	17	5	0	0	1	2	1	0	2	3	3	2	1	1	0	0	0	0
1.90	2.00	65	27	5	4	3	2	2	0	1	3	3	0	3	0	1	1	0	2	0
2.00	2.10	26	29	4	3	1	1	0	1	4	5	1	1	2	2	3	0	2	1	0
2.10	2.20	12	18	12	3	1	1	0	2	4	2	1	0	0	0	0	0	0	1	0
2.20	2.30	3	17	16	1	1	1	4	4	2	1	1	1	1	2	1	0	0	0	0
2.30	2.40	6	8	9	9	5	4	2	4	1	0	0	1	2	1	1	0	1	0	0
2.40	2.50	3	11	7	4	3	2	1	1	0	0	0	0	0	0	0	0	0	0	0
2.50	2.70	0	7	10	20	3	7	1	2	3	2	1	1	1	4	0	1	0	3	0
2.70	2.90	0	10	8	6	3	0	1	1	1	1	0	0	4	2	0	1	1	1	0
2.90	3.10	0	3	0	4	3	8	1	3	1	1	2	2	0	1	0	0	2	0	0
3.10	3.30	0	4	0	5	0	3	0	1	1	0	2	0	2	0	0	0	0	0	0
3.30	3.50	0	0	3	2	2	0	5	2	2	0	1	0	1	2	0	0	2	0	0
3.50	3.80	0	0	3	0	0	0	0	2	7	1	0	4	0	0	1	2	0	0	0
3.80	4.10	0	0	7	6	0	2	0	0	0	2	0	2	4	0	2	0	4	0	0
4.10	4.40	0	0	0	0	2	0	2	0	0	2	2	4	0	2	0	0	0	0	0
4.40	4.70	0	0	0	3	0	0	0	0	0	0	0	0	0	1	3	0	0	0	0
4.70	5.00	0	0	0	0	3	2	4	0	0	2	0	0	0	0	0	0	0	0	0
5.00	9.99	0	0	0	0	0	0	0	2	0	0	0	0	0	0	0	0	0	0	0

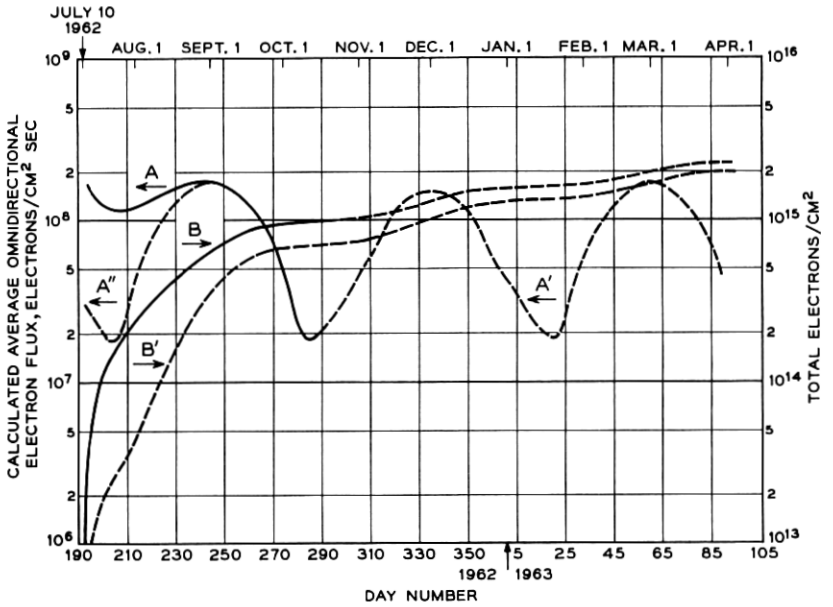

Fig. 23 — The exposure of the Telstar satellite to electrons. A fission beta-decay spectrum is assumed throughout space. The various curves are discussed in Section 2.4.2.

spectrum is everywhere that of fission fragment beta decay. The results are plotted in Fig. 23. When apogee is near the equator, the principal contribution comes from the high-intensity zone above $R = 1.7\ R_e$ and within 15 degrees of the magnetic dipole equator. When apogee is far north and south, the principal contribution comes from the higher-altitude portion of the passage through the equatorial region. In both cases, major contributions are made by regions on the high-altitude slope-off of the inner belt, where the spectrum definitely is softer than a fission spectrum, at least in later months. The total electron exposure as calculated is not substantially in error as far as electrons of 0.5 to 1 Mev are concerned. The total as plotted is probably too low to represent all electrons above 0 energy (or even 100 Kev) because of extra lower-energy electrons that are not shown in channel 3, but on the other hand it overestimates the flux of 1.5- or 2-Mev electrons if one applies to Fig. 23 the fraction of the fission beta spectrum that is appropriate to these higher energies.

The curves A and B represent the observed data from channel 3 with the assumed spectrum. From curve B we deduce that the Telstar

satellite experienced an average omnidirectional flux of 1.2×10^8 electron/cm^2 sec during its first 104 days in orbit. However, we point out that the instantaneous peak flux was 1.2×10^9 electrons/cm^2 sec and that the minimum instantaneous flux was substantially zero.

The curves A′, A″, and B′ make the additional assumption that the situation in mid-October prevailed between launch and March, 1963. The difference between curves A and A″ is due to those electrons which were observed to decay between July and October and hence seem certainly associated with the Starfish test. A large but still ill determined part of the remaining exposure, shown as curves A′, A″ and B′, is also attributable to Starfish electrons which are decaying much more slowly than those on the high-altitude side of the inner belt or in the slot between the inner and outer belts.

Substantial perturbations of the electron distribution were produced by a series of three Russian high-altitude nuclear tests on October 22, 28 and November 1. These additional electrons contributed significantly to the exposure of the satellite during late October and early November, when the exposure due to the natural electrons and those residual from Starfish, as indicated by curve A′, is relatively small. However, the effects of these electrons soon after they were produced were small in comparison with the peak exposure, such as shown by curve A′ for December 1. Furthermore, the Russian electrons disappeared relatively rapidly. The study of the detailed time dependence of the contributions of these three tests has not yet been completed.

2.4.3 *Integrated Proton Flux*

The *OCR* of the omnidirectional proton detectors have also been integrated. The results for protons between 26 and 34 Mev are presented in Fig. 24. Because the proton fluxes displayed so little temporal variation, the extrapolation to April, 1963, is more likely to be valid for protons than for electrons. The average *OCR* for this detector is 1.1×10^3 counts/cm^2 sec. The instantaneous *OCR* has a peak value of 1.5×10^4 counts/cm^2 sec and a minimum of zero. The curve A in this figure best displays the effect of the Brazilian anomaly. When apogee gets sufficiently far north, the orbit begins to go under the most intense region inside contour A of Fig. 17; this causes the dip in the average *OCR* centered at day 244. Owing to the Brazilian anomaly, the average position of the magnetic dipole equator is somewhat south of the geographic equator, and apogee does not get far enough south to make the dip pronounced on day 331. The asymmetry in the curve for the >50-

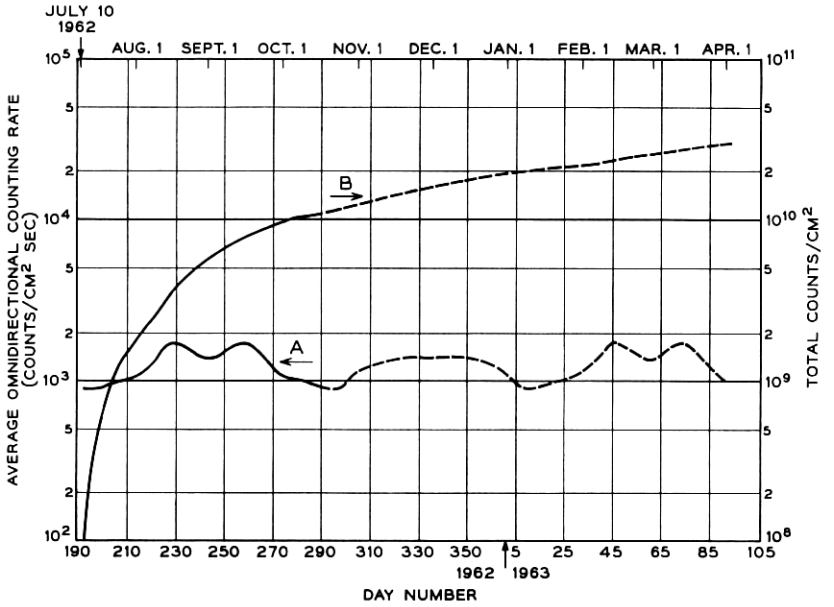

Fig. 24 — The exposure of the Telstar satellite to protons in the energy range 26 to 34 Mev. To convert to flux, multiply scales by 2.1. The curves are discussed in Section 2.4.3.

Mev proton detector is not as noticeable because here, as in the electron case, the central *OCR* contour extends to lower altitudes. The average *OCR* for protons above 50 Mev is 190 counts/cm^2 sec, as may be seen in Fig. 25. The range of observed instantaneous *OCR* is from 0 to 2500 counts/cm^2 sec. The conversion from *OCR* to flux is given in Section 2.3.

III. RADIATION DAMAGE AND SATELLITE COMPONENT EXPOSURE

The effects of radiation on the satellite fall into two broad classes. First, there are effects which arise from collisions of high-energy particles with the atoms of a solid in which sufficient energy may be transferred to create defects in the bulk of the solid. Immediately after a collision, the defects consist of vacancies where atoms are missing from normally occupied positions in the crystal and of interstitial atoms which occupy positions between the normal lattice sites. These defects are often highly mobile in the crystal and may recombine to restore the local crystal perfection or may become associated with one another or with other chemical or structural imperfections in the crystal. It is these combined

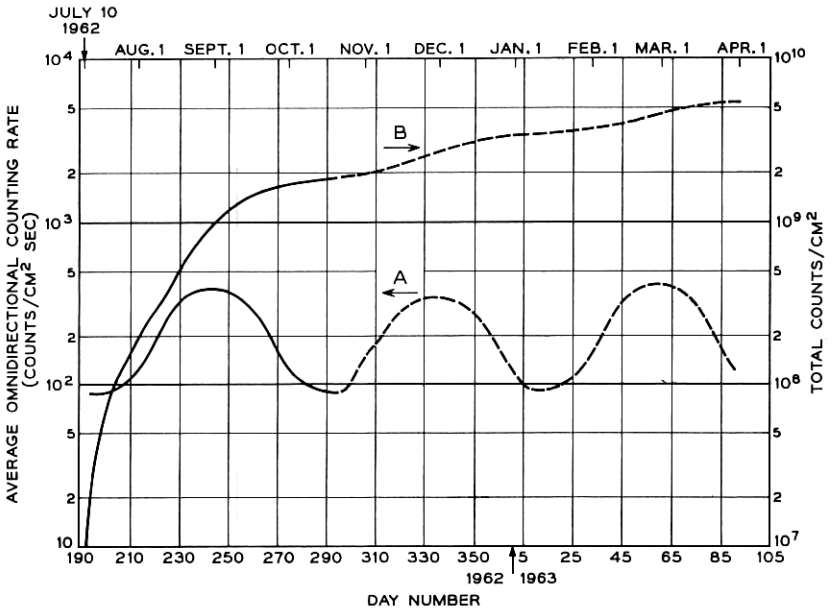

Fig. 25 — The exposure of the Telstar satellite to protons with energies above 50 Mev. To convert to flux, multiply scales by 2.6. The curves are discussed in Section 2.4.3.

centers that are in general stable at room temperature and give rise to radiation damage effects on the electrical, optical and structural properties of the material.[37,38] Such effects are produced in all solids. However, for semiconductor devices to operate, a high degree of perfection is required of semiconductor materials, and therefore radiation damage is usually much more important in semiconductor than in other solid-state materials.

The second broad class of radiation effects is produced by ionization due to high-energy charged particles. The ionization may be in the bulk of a solid and give rise to transient currents or provide electrons or holes that may be trapped at existing chemical or structural defects. The latter case is responsible for much of the coloration of transparent solids by radiation, an effect of negligible importance in the sapphire chosen for shielding the solar cells on the Telstar satellite. The ionization may cause chemical changes in organic plastics with resultant changes in their electrical and mechanical properties, and in the oil of capacitors with a resultant pressure build-up. By choice of materials, these effects have

been reduced to minor significance in the Telstar satellite. The ionization may also occur in gases, where it has been found to be of substantial importance if the gases are closely associated with semiconductor surfaces, as is often the case in encapsulated semiconductor devices. This latter effect, ionization damage to semiconductor devices, was recognized[39] and has proven to be of major importance in the performance of the satellite in space.

In this section of the paper, radiation damage (bulk effects) as observed in the semiconductor devices of the Telstar satellite will be considered in detail. The last parts of this section will discuss ionization to be expected at components in the canister of the satellite. The effects of this ionization on the component performance of the Telstar command decoder are discussed in another paper.[40]

3.1 *Measurements of Radiation Damage in the Satellite*

Radiation damage is measured directly in the solar power plant of the satellite, and in solar cells and specially fabricated transistors carried by the satellite for this experimental purpose. Solar cell results all depend upon the orientation of the sun with respect to the satellite, and thus the measurements of damage will be preceded by a description of the solar aspect determination made by the satellite.

3.1.1 *Solar Aspect*

As described in detail in a preceding paper,[1] the sun's orientation with respect to the satellite is determined by essentially simultaneous measurement of the output of six pre-irradiated silicon solar cells placed with their normals mutually perpendicular. The orientation can be described in terms of two angles: φ, the rotational angle or longitude of the sun in the coordinates of the satellite, and α, the colatitude of the sun measured with respect to the spin axis. Fig. 26 shows a sequence of measurements with the six aspect cells during an orbit on July 17, 1962. Because the spin rate of the satellite is not in general commensurate with the frame time of the telemetry, the particular cells which see the sun most directly change from frame to frame of the telemetry. In the case shown in Fig. 26, during each telemetry frame (approximately one minute), the satellite rotated by a number of complete rotations plus approximately 36 degrees. Thus, from frame to frame the readings gradually work through a sequence of rotational angles. Since the spin rate of the satellite gradually decreases (from its initial rate of approximately 180

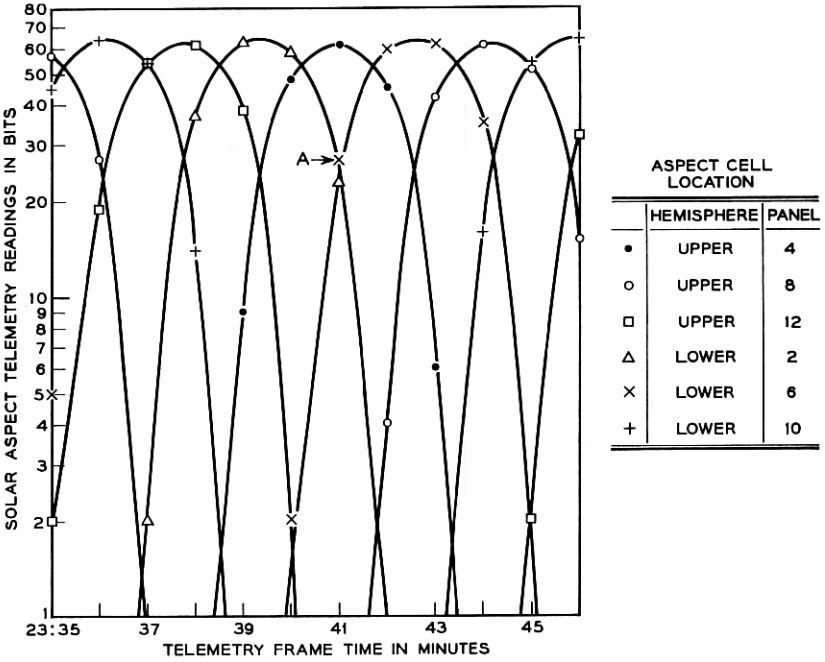

Fig. 26 — Telemetry bit readings of the six solar aspect cells on twelve successive frames of pass 70, July 17, 1962.

rpm at launch), this change in φ from frame to frame also changes. Furthermore, since this change in φ is measured at the end of a large number of complete rotations, the strobing of the solar aspect measurement gives a vernier measure on the rate of decay of the spin of the satellite. The accuracy of the measurement is limited by the accuracy of the telemetry frame time and by the accuracy of the determination of φ in a particular sequence of frames. No further discussion of this facet of the measurement will be included in the present paper.

The accuracy of the determination of the sun's position varies as the satellite rotates. At points such as A in Fig. 26, where three cells are prominently illuminated, α and φ can both readily be determined to within ± 0.5 degree. The data of the figure indicate that the sun is nearly on the equator of the satellite, since the peak outputs of the cells on the upper and lower hemispheres are nearly equal. The lower-hemisphere cells are reproducibly higher, however, and when calculated from these data, α is found to be 91.5 ± 0.5 degrees, measuring from the telemetry antenna end of the satellite.

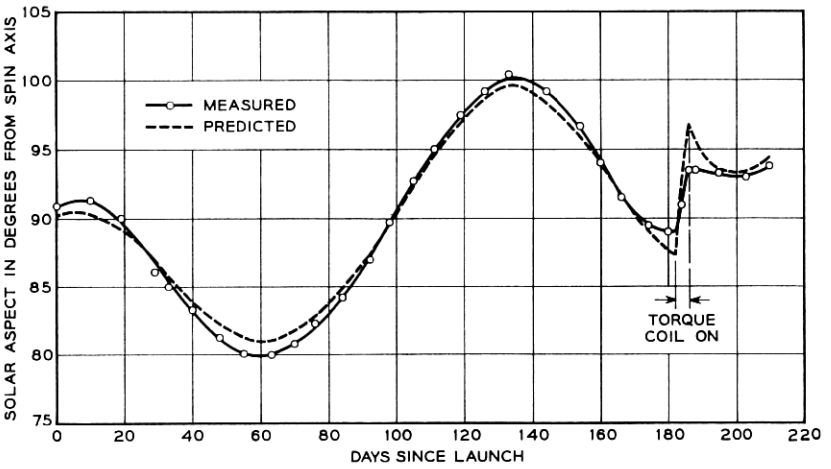

Fig. 27 — The time variation of α, the angle between the spin axis of the satellite and the satellite-sun line, from launch until February 5, 1963. The angle is measured from the telemetry antenna end of the satellite.

The history of the solar aspect of the satellite from launch to February, 1963, is shown in Fig. 27. The sun has been within ± 10 degrees of the equator at all times, a desirable position from the standpoint of temperature uniformity of the satellite and maximum capability of the solar power plant. The predicted curve illustrated here is discussed in an accompanying paper[41] dealing in more detail with satellite performance.

3.1.2 *Solar Power Plant*

Fig. 28 shows the output of the solar power plant of the satellite.[42] Since the distribution of solar cells is not uniform over the surface of the satellite, the telemetry reading which gives a momentary snapshot of the current from the power plant varies with φ and α. The data points of Fig. 28 have been derived from averages over a sequence of readings which, judging from the solar aspect measurements described in Section 3.1.1, represent a complete sampling over all values of φ. In cases for which the spin rate and telemetry frame rate are more nearly commensurate than in Fig. 26, a long sequence of readings will produce a cluster of points near some one or some several rotational angles. These cases have not been used in Fig. 28. Because small changes in the spin rate are reflected as large changes in φ at one-minute intervals, successive passes on the same day will exhibit quite different sampling characteristics. Data have also been selected for a particular battery voltage,

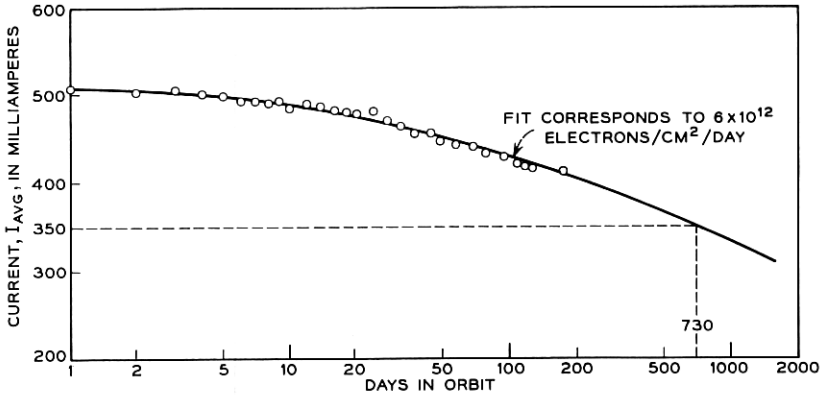

Fig. 28 — The average over the angle φ of the output current of the solar power plant from launch until February, 1963. Corrections have been made for mean solar distance. No detailed temperature corrections or corrections for solar aspect angle have been made in these data. Such corrections are expected to reduce the scatter of the points.

since the current which the power plant supplies depends on the load into which it is working. The chosen voltage corresponds to 0.36 volt/cell in the series solar-cell strings. The solar power plant current, selected in this way and averaged over φ, has been corrected for mean solar distance to give the points plotted.*

The solar power plant output will decrease due to radiation damage of silicon by energetic particles capable of penetrating the 0.3 gram/cm^2 sapphire shielding which covers the solar cells. The observed damage can be expressed in terms of an equivalent flux of 1-Mev electrons which would have produced this damage in the laboratory under conditions of normal incidence and zero shielding. The term "1-Mev equivalent flux" will be used for this measure of damage. The curve fitted through the points of Fig. 28 corresponds to a 1-Mev equivalent flux of 6×10^{12}/cm^2 day. This fitting implies that the damage flux encountered by the satellite is constant in time, in contrast to the oscillatory radiation exposure of the satellite discussed in Section 2.4. The accuracy of the solar cell data does not permit such a conclusion to be drawn, however, and the fit of Fig. 28 represents an equivalent flux averaged over 100 or more days in orbit. The choice of 6×10^{12} in this fit is at least accurate to within a factor of 1.5. The extrapolation of the curve indicates, as shown in the figure, that after two years the solar power plant will have degraded to 68 per cent of its initial performance.

* These considerations are discussed in more detail in Ref. 42.

3.1.3 *Solar Cell Damage*

Three solar cells with different shielding thicknesses were flown to measure radiation damage. Their outputs are sampled at the same time as the outputs of the solar aspect cells, Section 3.1.1, and the damage cells have the same orientation with respect to the sun as the aspect cell on panel 12 of the upper hemisphere of the satellite. Thus, no corrections for angle of illumination are required in recognizing the presence of damage. The ratio of the output currents of the damage-measuring cells to that of the pre-irradiated aspect cell on panel U-12 are shown in Fig. 29. The initial ratios are within ±2 per cent of those anticipated from laboratory calibrations of the spectral response of the cells and calculation of their performance under outer space illumination.

The currents of the initially unirradiated cells degrade with time in orbit and after a few days are ordered in accordance with their shielding thicknesses. The lack of order in the earliest days is due entirely to the slightly different initial outputs of the three individual devices. The shapes of the three curves are very similar, although there is some scatter in the data due in large measure to the approximately ±1 per cent digitizing accuracy of the telemetry. The shapes of the curves are not what would be expected from a constant particle exposure and indicate a minimum in the damage rate between approximately 70 and 110 days after launch. This corresponds reasonably well with the minima in radiation exposure shown on Figs. 23 to 25. The damage sensitivity

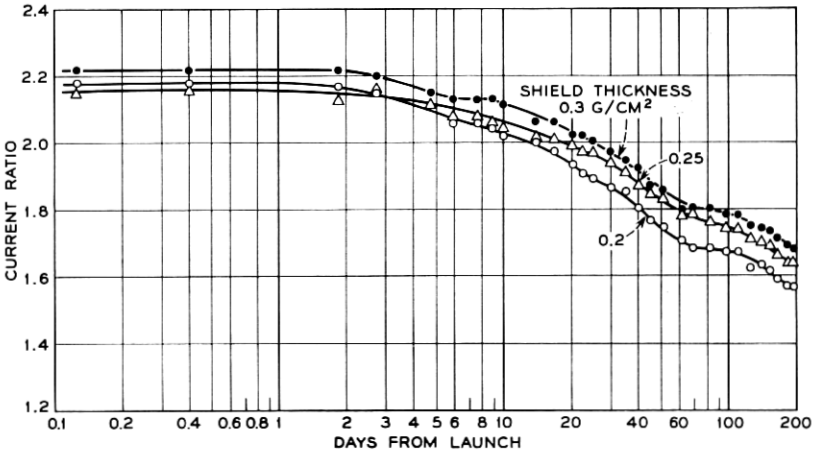

Fig. 29 — The ratios of the output currents of the radiation damage solar cells to the pre-irradiated aspect cell on satellite panel upper 12.

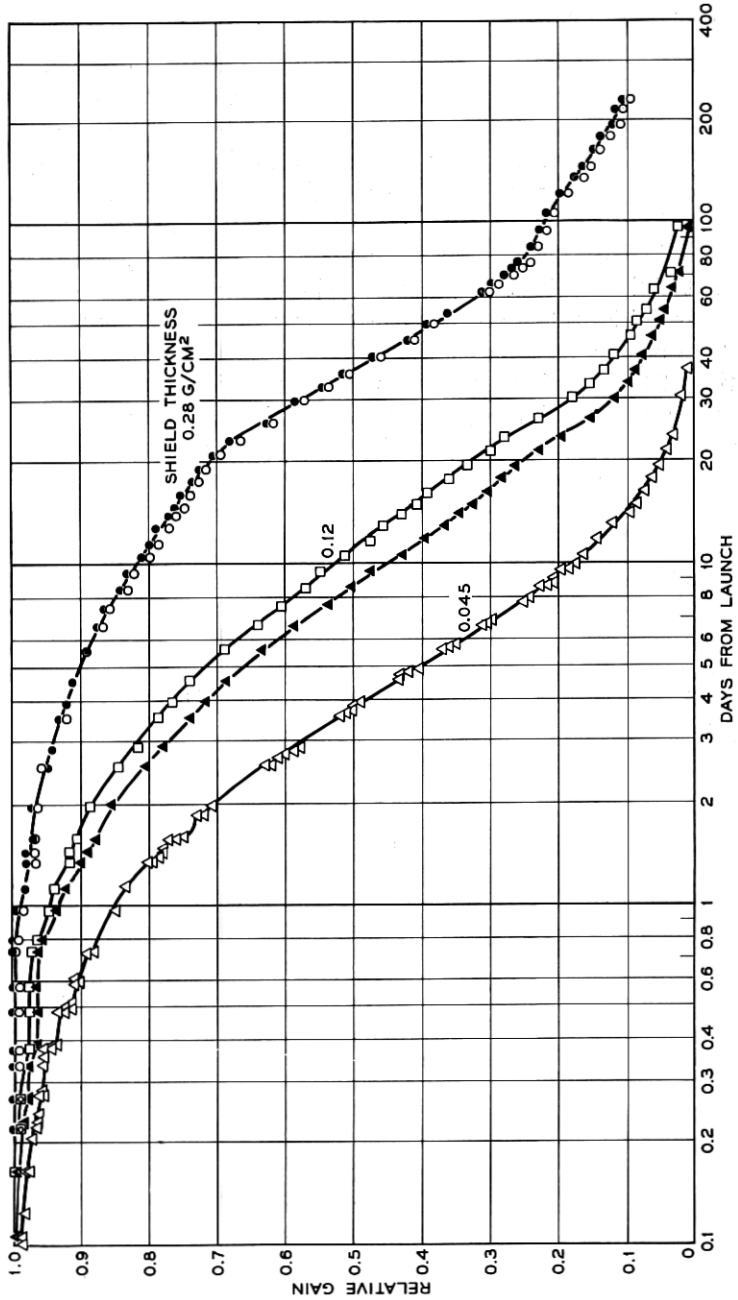

Fig. 30 — The relative gains of the radiation damage transistors as a function of time.

of the 0.20 and 0.30 gram/cm² shielded devices differs by approximately a factor of 2, with the 0.25 gram/cm² shielded cell falling between these extremes.

3.1.4 *Damage Transistors*

A group of specially fabricated n-p-n transistors with unusually wide base regions provides an independent measure of radiation damage to silicon with advantages in comparison to solar cells that light is non-essential and that sensitivity to damage is quite high. These devices are described in a previous paper.[1] The common-base current gain of these transistors is directly related to the lifetime of holes in the p-type base region and thus to the additional recombination centers added by radiation damage. This is the same property which is of major importance to damage in solar cells.

Fig. 30 shows the current gain of the transistors, normalized by their initial gain values. The initial gain ranged for this group of devices between 0.40 and 0.48, but examination of the theory indicates that a normalized gain scale retains very little sensitivity to the actual initial gain values. Five devices provide the essential data of Fig. 30, two each at two shield thicknesses and one at a third. The shield of these transistors is made up partly (and in the most lightly shielded case, totally) of the 3-mil Kovar lid of an encapsulating can and partly of additional aluminum. The thickness indicated on the curves is the aluminum shielding which would be equivalent to the sum of these, taking into account the relative mass stopping power of the two materials for protons.

All of the curves of Fig. 30 have similar S-shapes. If the devices followed a simple form of the theory, the curves should be closely related to the hyperbolic secant of the square root of the damaging flux, or if the flux is constant in time, to the square root of the abscissa of Fig. 30. This is only very roughly the case. In the 0.045 gram/cm² shielded device, the decrease observed during the first two days in orbit exhibits some clear downward steps. These steps are larger than those to be expected from changes of the telemetry reading by a single bit. They are associated with passages of the satellite through the inner radiation belt. The separation of the steps is a minimum of about 0.1 day, or approximately the orbital period of the satellite. Similar changes cannot be discerned beyond two days in orbit for this transistor or at any time for the more heavily shielded devices. This is a result in both cases of too low a sensitivity to detect such behavior, although it must occur. On the most heavily shielded pair of transistors there is a definite indica-

tion that the damage rate increases in the region between 25 and 70 days, decreases between 80 and 110 days, and increases again at longer times. This is suggestive of the oscillations in radiation exposure illustrated in Figs. 23 to 25. The more lightly shielded devices have been so severely degraded by these times that it is not possible to draw similar conclusions from their data. The relative damage sensitivity of the devices, as represented by their separation on the log time scale, varies only a small amount for relative gains between 0.9 and 0.2. Comparing the least and most heavily shielded devices, these ratios range from approximately 9 to 12, with the larger number being clearly too high because of the jog in the curve between 80 and 110 days. The average response of the intermediate-shielded transistors, compared with the heavily shielded pair, shows a relative sensitivity to radiation of between a factor of 3.5 and 4.5 over this same range in normalized gain. The effective damaging flux versus time could be deduced for each of the devices essentially by differentiation of the plotted curves. The data do not seem to be capable of providing this detailed a result, however, and although the variations in slope of the curves are evident as noted above, the magnitude of these variations cannot be deduced with any significant accuracy. The data have been used to specify the relative effectiveness of shielding or the relative sensitivity of differently shielded devices to radiation damage in the Telstar orbit.

3.1.5 *Composite Damage vs Shielding*

The results of the solar cell damage and transistor damage experiments have been combined in Fig. 31. The damage rate for the 0.30 gram/cm^2 shielded solar cell has been selected as unity and the other solar cells referred to it. The most heavily shielded transistors (0.28 gram/cm^2) have been placed at an ordinate interpolated between the 0.30 and 0.25 gram/cm^2 solar cell results. The other transistors have been placed by reference to the most heavily shielded pair. The increase in damage rate with decreasing shielding in the Telstar orbit is more than a factor of 10 over the range examined. This range extends from the sapphire shield of the Telstar power plant to shielding approximately equivalent to the 6-mil glass microsheet often used in the solar power supplies of lower-altitude satellites. If very thin solar cell shields had been used on the Telstar satellite, the two-year extrapolated performance of the power plant would have been realized in about 2.5 months. Furthermore, if p-on-n rather than n-on-p solar cells had been used in the power plant, this extrapolated end-of-life power would have been reached

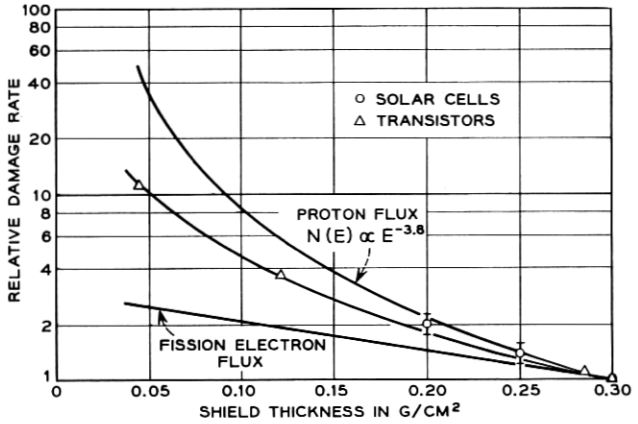

Fig. 31 — The composite results for radiation damage rate vs shielding thickness as determined from the solar cell and transistor damage experiments.

after about two or three weeks in space. The increase in damage with decrease in shielding can arise from either the proton or the electron component of the radiation environment. The two remaining curves of Fig. 31 bear on this question and will be discussed in detail in Section 3.2.3.

3.2 *Correlation of Particle Exposure and Observed Damage*

In this section the effects of the Van Allen belt particles on damaging n-on-p silicon solar cells will be considered, first in general and finally specifically in terms of the radiation exposure of the Telstar satellite as mapped out by its particle detectors and computed by integrating over the satellite orbit.

3.2.1 *Proton Damage vs Energy and Shielding*

A great deal of experimental data has been obtained on the changes in characteristics of n-on-p solar cells under bombardment by electrons and protons of different energies.[43-46] The experiments have generally been carried out with particles brought in at normal incidence to unshielded solar cells. These data, together with an understanding of the penetration characteristics of particles through shield materials, provide the basis for constructing the equivalent damage flux in the sense of Section 3.1.2 for any particle energy distribution and shielding configuration of a solar cell array.

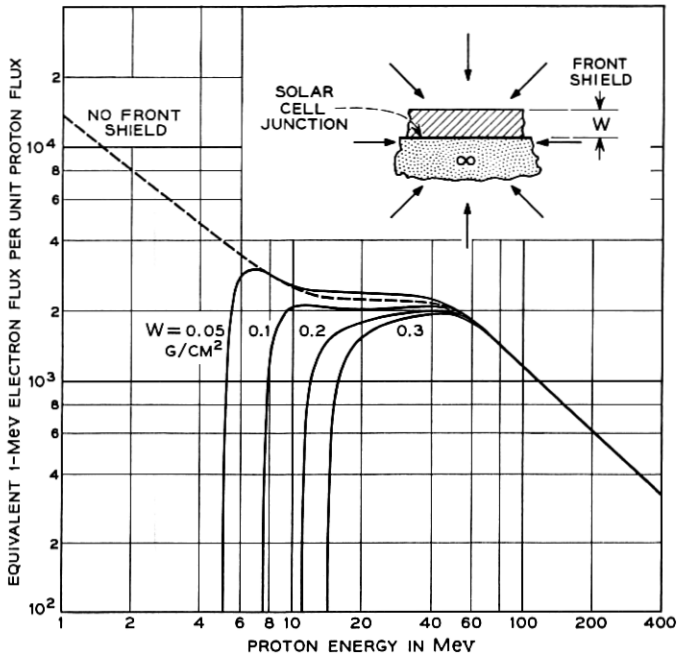

Fig. 32 — The damage-equivalent 1-Mev electron flux as a function of the energy of a monoenergetic isotropic flux of protons incident on n-on-p solar cells with various front shielding. The back shield is assumed to be infinitely thick.

Fig. 32 shows the 1-Mev electron flux equivalent in damage to a monoenergetic isotropic proton flux at different energies and for different shielding thicknesses. The curve for "no front shield" is a smooth curve with a shape determined by data obtained at four different proton particle accelerators and at seventeen different energies over the energy range between 1.4 and 135 Mev. It has been extrapolated with only minor uncertainty at both ends, although particles in the extrapolated extremes have a negligible effect on damage in the Telstar satellite case. The absolute ordinate scale for this curve differs from the data by exactly a factor of 2. As noted in the inset to the figure, the incident flux is assumed to be omnidirectional and uniform, and in all cases the solar cell is considered to have effectively infinite shielding on the back. This represents the actual situation in the Telstar solar power plant quite well. In this case, only one-half of all the protons in the incident flux can reach the solar cell, hence the factor of 2. The simplicity of this factor involves another approximation. Particles arriving at non-normal

incidence have longer paths in the solar cell and as a result create proportionately more defects in the radiation-sensitive thickness of the device. This introduces a $1/\cos\theta$ factor, where θ is the angle of particle incidence, which just cancels the $\cos\theta$ factor that reduces the proton flux because of the change in projected area of the device at an angle θ. As long as the sensitive thickness, t, is small enough so that $t/\cos\theta$ is small compared with the proton range, this approximation is good. At very low proton energies and at large angles of incidence, however, this approximation breaks down. For the sensitive thickness of the n-on-p solar cells used in the Telstar power plant, this approximation begins to be poor below about 5 Mev. One final reservation needs to be made concerning these data. The solar cell property that is being affected by the radiation damage in these experiments is the diffusion length for electrons in the p-type silicon base of the solar cell. This property controls the efficiency with which hole-electron pairs created by light in the base material can reach the p-n junction and contribute current to an external load.[44] This property change exhibits itself directly in a decrease in the short-circuit current of solar cells as a result of radiation. This effect is the primary cause of degradation in solar cell performance in the Telstar satellite. It is not, however, the only effect that occurs. There is a change in junction impedance that shows up as a decrease in open-circuit voltage, and there is a change in the temperature coefficient of the solar cell because of the introduction of new recombination centers. Although these are of minor importance in the Telstar case, they are not always of minor importance for other solar power plant designs. In particular, recent experiments have shown very severe damage to the junction impedance by very low energy, <1-Mev protons.[46] For unshielded solar power plants and possibly for very lightly shielded cases as well, this effect could be of major significance. Furthermore, if the power plant has not been designed for maximum power after radiation damage, including the modified temperature coefficient of the solar cells, the particular operating point may emphasize the changes in junction voltage.[42]

The shape of the basic proton energy dependence of damage, as illustrated by the upper curve of Fig. 32, is still not quantitatively understood. The straight line portions at low and high energies have slopes that agree very well with the theory of atomic displacements[47] by heavy charged particles. The offset in these two line segments, produced by the nearly energy-independent portion between about 10 and 40 Mev is, however, still a subject of discussion.[45,48,49] The same energy dependence, but with a difference in absolute magnitude, is also found for

proton damage in p-on-n solar cells. The shape seems most likely to be determined by details of the short-range interaction of energetic protons with atoms of the silicon lattice.

Starting with the upper curve of Fig. 32, the other curves in the figure have been generated by machine computation, taking into account the penetration properties of protons. For each shield thickness, the equivalent damage flux rises sharply with increasing proton energy as the protons are capable of penetrating the shield. The curves then join with the unshielded curve at higher energies. One might expect that because lower-energy protons are more damaging, the introduction of shielding, which would reduce the proton energy for those protons capable of penetrating the shield, might increase rather than decrease the damage. However, because the protons are incident over all angles, the very severe limitation of the solid angle available to protons that go through the shield and have a small residual energy reduces what must be a real effect to relative unimportance. The effect does appear as a small crossing of the equivalent flux curves for the unshielded and most lightly shielded cases. The Telstar radiation damage experiments discussed in Section 3.1 covered just the range of shields illustrated in Fig. 32. The main solar power plant with 0.3 gram/cm^2 sapphire shielding is sensitive only to protons of more than 15 Mev. The most lightly shielded damage transistors respond to protons of more than 5 Mev. Because the damage per particle is high at lower energy, and because there are more protons in the Telstar orbit with lower energies, a reduction in shielding is expected to effect a large increase in damage.

3.2.2 *Electron Damage vs Energy and Shielding*

Fig. 33 shows a set of curves for electron damage having the same significance as those for protons of Fig. 32. These curves are based on measurements made of damage at different angles of incidence and thickness of shielding with electrons up to 3 Mev.[50] The uniformity in variation of the results with the extrapolated range of electrons has permitted extension of the shielding calculations to higher energies. In all cases the damage increases with increasing electron energy in contrast to the decrease with increasing proton energy. For the "no front shield" curve, the rapid fall-off below 1 Mev reflects the fact that electrons are relatively inefficient in moving atoms in the silicon crystal to produce damaging defects and at low energies become nearly incapable of transferring enough energy to the atoms for them to be displaced. The shape of the curve is very roughly in accord with theoretical expectation below

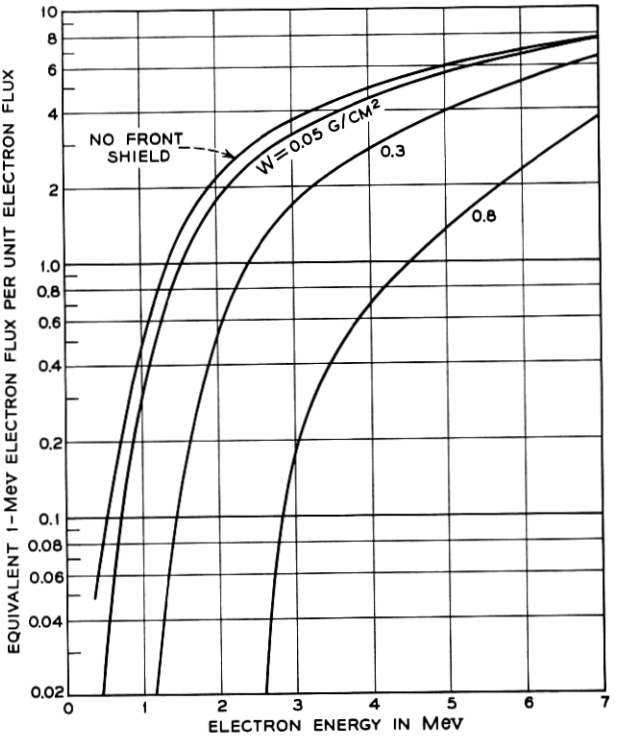

Fig. 33 — The damage-equivalent 1-Mev electron flux as a function of the energy of a monoenergetic isotropic flux of electrons incident on n-on-p solar cells with various front shielding. The back shield is assumed to be infinitely thick.

1 Mev. Above 1 Mev the simple theory of atomic displacement predicts that the curve should flatten out without much further increase at higher energies.[47] The experimental data from which the curve was drawn, however, show more than a factor of 10 increase between 1 and 7 Mev.* The situation for p-on-n solar cell damage is quite different in this respect, the increase above 1 Mev being much more nearly in accord with the simple theory. Apparently the high damage efficiency for high-energy electrons in p-type silicon is due to the formation of a different type of damage defect in the crystal which is very efficient as a recombination center. It is plausible that this new defect is a divacancy.[52]

The equivalent 1-Mev damage flux for 1-Mev electrons is 0.5 in Fig.

* The data above 3 Mev for no front shield are due to J. M. Denney and R. G. Downing, Ref. 51.

33 because of rejection of half of the electrons in an omnidirectional flux by the assumed infinite back shielding. There is an additional effect of reflection of electrons (back scattering) from the surface of the silicon for high angles of incidence that tends to reduce the value to less than 0.5, but this effect is quite small. The Telstar solar power plant, with 0.3 gram/cm^2 shielding, begins to be severely damaged by electrons in the 1- to 2-Mev region, while transistors shielded by 0.045 gram/cm^2 are similarly damaged by electrons of 0.5 to 1.0 Mev energy. Even for these lightest shields, electrons below 0.5 Mev become rapidly insignificant.

3.2.3 *Composite Damage from the Satellite Exposure*

Two factors in the Telstar radiation damage results will be considered in this section: first the damage vs shielding thickness of Fig. 31, and second the absolute magnitude of the damage to the solar power plant as described in Section 3.1.2. It is evident from the curves of Figs. 32 and 33 that the energy spectra of the protons and electrons encountered by the satellite are of enormous importance in both of these respects.

The proton spectrum varies with position in space as discussed in Section 2.3.2, and this spectrum change could have been included in carrying out the initial orbital integrals. However, from the 100-day average exposure of the 26 to 34 Mev protons, Fig. 24, and the >50-Mev protons, Fig. 25, we have instead deduced an average spectrum for the exposure. This average spectrum has the same significance as the spectrum derived for any single point in space. It is characterized by (1) in Section 2.3.2 with $n = 3.8$, a value which is intermediate between the $n \approx 2$ for the heart of the inner belt and $n \approx 4.5$ for the outer side of the inner belt. The average spectrum has been derived over approximately half a period of the precession of the line of apsides, Fig. 20; and since the proton flux is essentially constant in time, the average should reflect the situation for longer times as well.

The spectrum above has been folded through the curves of Fig. 32 to obtain the dependence of the proton damage on shielding thickness. The result is the upper curve of Fig. 31, which has been normalized to the 0.3 gram/cm^2 point. This curve asserts that if the damage at 0.3 gram/cm^2 shielding is due entirely to protons, then the damage should increase at thinner shields as shown. The actual observations lie everywhere below this computed curve, suggesting tentatively that protons may not be responsible for all the damage at 0.3 gram/cm^2. Because of the extrapolation involved in including protons as low as 5 Mev in energy, the calculation for lower shield thicknesses becomes increasingly

uncertain. However, from an as yet incomplete analysis of Telstar and Explorer XV low-energy proton data, the 5-Mev proton exposure derived from the average spectrum seems to be correct to within approximately a factor of 2.

Because of the very important contribution of high-energy electrons to the damage and the inability of the Telstar electron detector to specify their spectrum above 1 Mev, the electron case is more difficult. There is no doubt that a substantial part of the Telstar electron exposure came from regions where the electron spectrum was characteristic of fission beta decay (Section 2.2.2). However, a substantial part of its exposure also came from regions in which there is little doubt that the spectrum contained a smaller fraction of high-energy electrons than the fission spectrum. For lack of more complete knowledge, we have assumed the spectrum is fission-like throughout and recognize that this overestimates the high-energy part of the average electron spectrum. Folding this spectrum through the curve of Fig. 33, the lowest curve of Fig. 31 is obtained. This curve is fitted, as in the proton case above, at the 0.3 gram/cm^2 point under the assumption that at that point all the damage is due to electrons with a fission spectrum. In this case the calculation falls everywhere below the observations. The calculated curve is relatively flat because fission electrons are so energetic. The electron spectrum could, of course, be adjusted to fit the actual observations by adding electrons between 0.5 and 1.0 Mev. However, this is the energy range in which the Telstar electron detector is measuring the flux of particles, and there are altogether too few electrons under the assumption of such a soft spectrum to allow electrons to contribute in a major way to the damage at any thickness of shielding.

The fact that the observations fall between the electron and proton predictions suggests that the actual situation contains important contributions from both types of particles. A half-and-half sharing of the damage at 0.3 gram/cm^2 nearly accounts for the points at lesser shielding. For the thinnest shield, such a computation gives a result a factor of approximately 2 above the point; however, this is the region in which the proton damage is subject to an uncertainty of about this magnitude.

Using the same spectral assumptions discussed above and the computed average of the particle exposure of the satellite, Figs. 23 to 25, the absolute damage to be expected in the solar power plant can be obtained. The damage from the proton exposure averaged over 100 days in orbit is found to be equivalent to that which would be produced by 3×10^{12} 1-Mev electrons/cm^2 day at normal incidence on bare n-on-p solar cells. A similar calculation for electrons gives the same results, although in this case the spectral assumption is such as to overestimate

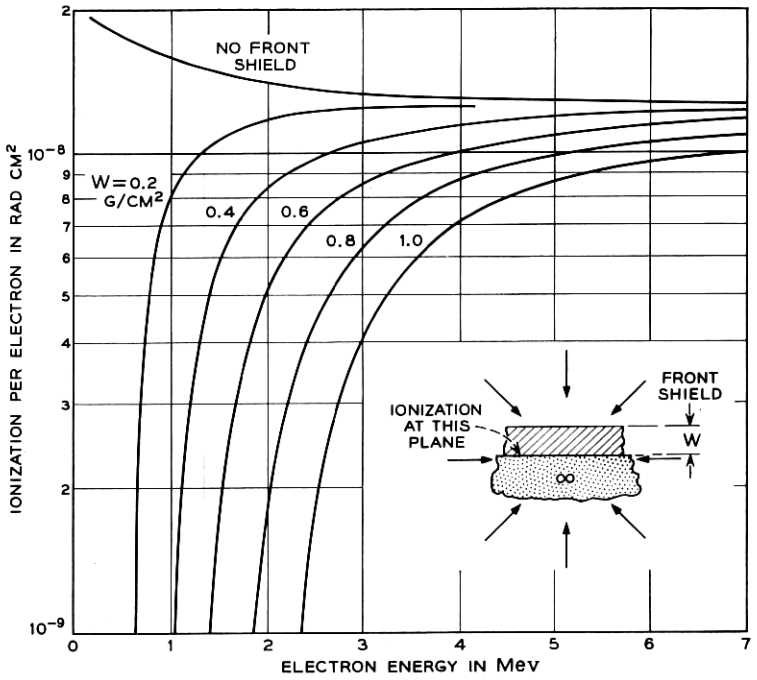

Fig. 34 — Ionization produced by a monoenergetic isotropic flux of electrons behind various thicknesses of front shielding. The back shield is assumed to be infinitely thick.

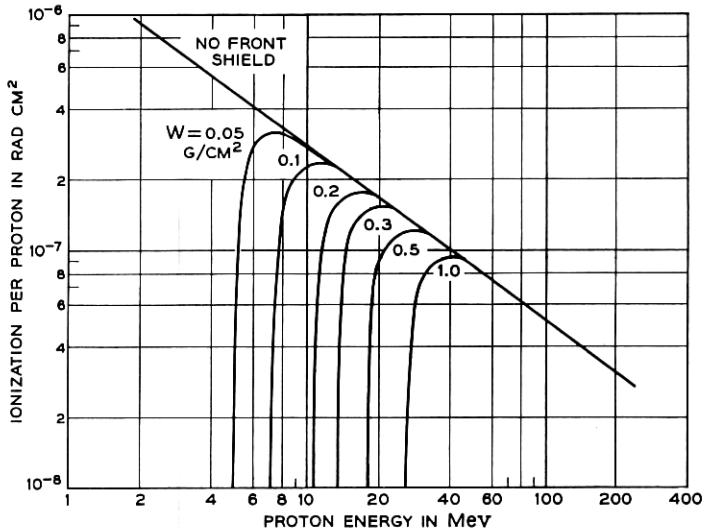

Fig. 35 — Ionization produced by a monoenergetic isotropic flux of protons behind various thicknessess of front shielding. The back shield is assumed to be infinitely thick.

the electron damage. To the accuracy with which this calculation has presently been carried out, it is possible to account for the observed damage by an equivalent 1-Mev electron flux of $6 \times 10^{12}/\text{cm}^2$ day, half of which is produced by protons and half by electrons. This composite also provides a satisfactory fit to the dependence of damage on shielding thickness. The electron contribution in this calculation is higher than that quoted in an earlier paper[18] because recently measured damage by high-energy electrons to n-on-p solar cells is considerably greater than had been anticipated from measurements at lower energies which were used in the earlier computation.

3.3 *Radiation of Circuit Components in the Satellite Canister*

The calculation of the radiation exposure of the satellite has made it possible to explain the changes in characteristics that have been observed in the silicon solar cells and the closely related damage transistors. In this section we will examine the exposure from the standpoint of the ionization (rather than the bulk semiconductor damage) it produces under different thicknesses of shielding. The results are applicable, for example, to ionization damage in the transistors of the Telstar command decoder.

3.3.1 *Ionization Due to Electrons and Protons*

Fig. 34 shows the ionization as a function of electron energy in an isotropic monoenergetic electron flux. The geometry of the case considered is indicated in the inset to the figure. A typical point on this set of curves is to be interpreted as follows. In an omnidirectional flux of 10^7 2-Mev electrons/cm^2 sec incident on a semi-infinite slab of material, the ionization level would be $5 \times 10^{-9} \times 10^7$ rads/sec or 1.8×10^2 rads/hr at a depth of 0.6 gram/cm^2.

Fig. 35 shows a similar set of curves for protons. There is more ionization per particle in this case because the protons are not minimum-ionizing. Beyond the right-hand extreme of the proton curves, the ionization converges to the same value per particle as for the electrons, the protons now being relativistic in velocity and minimum-ionizing in their interaction with materials.

3.3.2 *Composite Ionization from the Integrated Satellite Exposure*

With the same average particle spectra as used in Section 3.2.3 to compute the radiation damage to solar cells, the ionization due to elec-

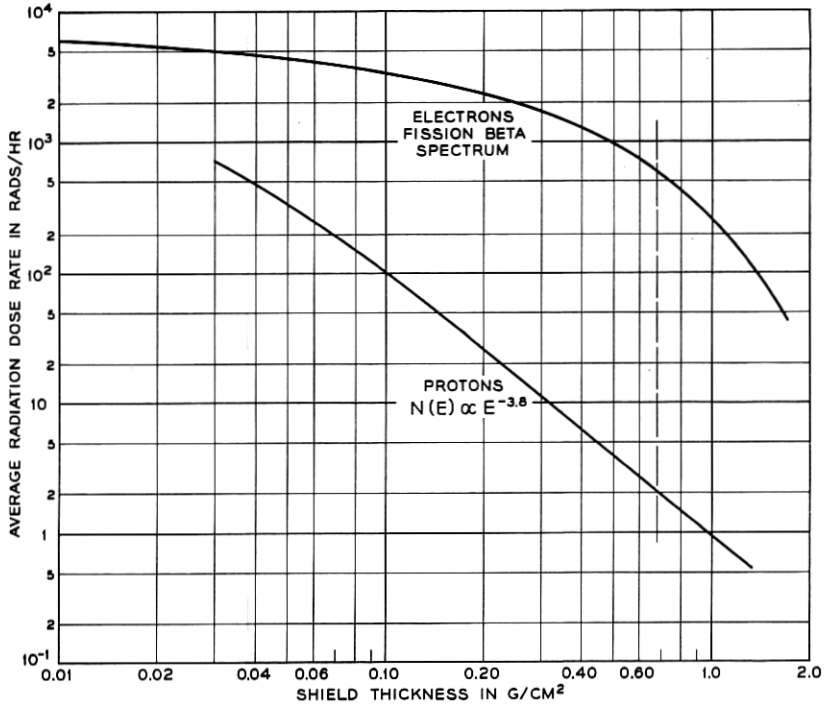

Fig. 36 — Average radiation dose rate vs shielding thickness for the average proton and electron exposure of the satellite.

trons and protons has been derived from the curves of Figs. 34 and 35. The results are shown in Fig. 36. At a shielding thickness of 0.68 gram/cm² (0.1 inch of aluminum, the approximate location of the Telstar decoder transistors) only protons of >20 Mev and electrons of >1.5 Mev are important. At this thickness the electron contribution to the radiation is about 600 rads/hr compared with 2 rads/hr from the protons. The proton-produced intensity is nearly what had been expected before launch, but the more than two orders of magnitude additional ionization contributed by the penetrating electrons were totally unexpected and were responsible for the failure of the Telstar command decoder.[40]

IV. ACKNOWLEDGMENT

We are deeply appreciative of the efforts of many people who have contributed greatly to this work. In particular we are grateful to Miss

E. M. Engert, who had a major role in the data reduction; Mrs. M. F. Robbins, who wrote many of the plot programs; R. L. Stickle, who decommutated the telemetry data, and Mrs. P. L. Gibbs, who edited it; L. C. Thomas, who supplied the satellite spin axis orientation and most of the ephemeris, and F. T. Geyling and G. J. Miron, who supplied the remainder; D. B. Cuttriss, who reduced the solar power plant data; D. W. Hill, who organized the program for reduction of solar aspect data; and L. V. Medford, who carried out this reduction as well as that for the radiation damage solar cells and transistors.

We especially acknowledge the participation of the NASA world-wide tracking network which recorded more than half of the telemetry acquired from the Telstar satellite.

REFERENCES

1. Brown, W. L., Buck, T. M., Medford, L. V., Thomas, E. W., Gummel, H. K., Miller, G. L., and Smits, F. M. The Spacecraft Radiation Experiment, B.S.T.J., this issue, p. 899.
2. Welch, J. A., Jr., and Whitaker, W. A., Theory of Geomagnetically Trapped Electrons from an Artificial Source, J. Geophys. Res., **64,** 1959, p. 909.
3. Northrop, T. G., and Teller, E., Stability of the Adiabatic Motion of Charged Particles in the Earth's Field, Phys. Rev., **117,** 1960, p. 215.
4. Northrop, T. G., The Guiding Center Approximation to Charged Particle Motion, Ann. Phys., **15,** 1961, p. 79, and references therein.
5. Hess, W. N., Canfield, E. H., and Lingenfelter, R. E., Cosmic Ray Neutron Demography, J. Geophys. Res., **66,** 1961, p. 665.
6. Dessler, A. J., and Karplus, R., Some Properties of the Van Allen Radiation, Phys. Rev. Letters, **4,** 1960, p. 271.
7. Walt, M., and MacDonald, W. M., Diffusion of Electrons in the Van Allen Radiation Belt, J. Geophys. Res., **67,** 1962, p. 5013.
8. Welch, J. A., Jr., Kaufmann, R. L., and Hess, W. N., Trapped Electron Time Histories for $L = 1.18$ to $L = 1.30$, J. Geophys. Res., **68,** 1963, p. 685.
9. Ray, E. C., On the Theory of Protons Trapped in the Earth's Magnetic Field, J. Geophys. Res., **65,** 1960, p. 1125.
10. Lenchek, A. M., and Singer, S. F., Geomagnetically Trapped Protons from Cosmic-Ray Albedo Neutrons, J. Geophys. Res., **67,** 1962, p. 1263.
11. Pizzella, G., McIlwain, C. E., and Van Allen, J. A., Time Variations of Intensity in the Earth's Inner Radiation Zone, October 1959 through December 1960, J. Geophys. Res., **67,** 1962, p. 1235.
12. Kaufmann, R., Experimental Tests for the Acceleration of Trapped Particles, J. Geophys. Res., **68,** 1963, p. 371.
13. O'Brien, B. J., A Large Diurnal Variation of the Geomagnetically Trapped Radiation, J. Geophys. Res., **68,** 1963, p. 989.
14. O'Brien, B. J., Direct Observations of Dumping of Electrons at 1000 Kilometer Altitude and High Latitudes, J. Geophys. Res., **67,** 1962, p. 1227.
15. McIlwain, C. E., Coordinates for Mapping the Distribution of Magnetically Trapped Particles, J. Geophys. Res., **66,** 1961, p. 3681.
16. McIlwain, C. E., private communication, June, 1962.
17. Chapman, R. C., Jr., Critchlow, G. F., and Mann, H., Command and Telemetry Systems, B.S.T.J., this issue, p. 1027.
18. Brown, W. L., and Gabbe, J. D., The Electron Distribution in the Earth's Radiation Belts during July 1962 as Measured by Telstar, J. Geophys. Res., **68,** 1963, p. 607.
19. Carter, R. E., Reines, F., Wagner, J. J., and Wyman, M. E., Free Antineutrino

Absorption Cross Section, Expected Cross Section from Measurements of Fission Fragment Electron Spectrum, Phys. Rev., **113,** 1959, p. 280.
20. Van Allen, J. A., Frank, L. A., and O'Brien, B. J., Satellite Observations of the Artificial Radiation Belt of July 1962, J. Geophys. Res., **68,** 1963, p. 619.
21. Van Allen, J. A., Absolute Intensity, Spatial Distribution and Time Decay of Intensities of Artificially Injected Electrons Based on Observations with Injun I, Explorer XIV, Injun 3, and DOD Satellites, Program of the 44th Annual Meeting of the American Geophysical Union (April 17, 1963), p. 76.
22. Brown, W. L., Hess, W. N., and Van Allen, J. A., Collected Papers on the Artificial Radiation Belt from the July 9, 1962 Nuclear Detonation. Introduction, J. Geophys. Res., **68,** 1963, p. 605.
23. McIlwain, C. E., Trapped Electron-Proton Intensities as Functions of Energy, B, L, and Time, Program of the 44th Annual Meeting of the American Geophysical Union (April 17, 1963), p. 76.
24. Brown, W. L., Trapped Particle Population from Telstar and Explorer XV Observations, Program of the 44th Annual Meeting of the American Geophysical Union (April 17, 1963), p. 76.
25. Hess, W. N., Injection and Loss Problems, Program of the 44th Annual Meeting of the American Geophysical Union (April 17, 1963), p. 76.
26. Whitaker, W. A., private communication, April 1963.
27. Pieper, G. F., Williams, D. J., and Frank, L. A., TRAAC Observations of the Artificial Radiation Belt from the July 9, 1962 Nuclear Detonation, J. Geophys. Res., **68,** 1963, p. 635.
28. West, H. I., Jr., Mann, L. G., and Bloom, S. D., Spectra and Fluxes of Electrons Trapped in the Earth's Magnetic Field Following Recent High-Altitude Nuclear Bursts, Program of the 44th Annual Meeting of the American Geophysical Union (April 17, 1963), p. 77.
29. Giacconi, R., Paolini, F. R., and Katz, L., Measurements of Trapped Particles Injected by Nuclear Detonations, Program of the 44th Annual Meeting of the American Geophysical Union (April 17, 1963), p. 77.
30. White, R. S., Freden, S. C., Mihalov, J. D., Mozer, F. S., and Paulikas, G. A., The Artificial Radiation Belts at Low Altitudes, Program of the 44th Annual Meeting of the American Geophysical Union (April 17, 1963), p. 77.
31. Smith, R., Electron Flux Measurements from DOD Satellites During the Period July to November 1962, Program of the 44th Annual Meeting of the American Geophysical Union (April 17, 1963), p. 76.
32. Van Allen, J. A., The Geomagnetically Trapped Corpuscular Radiation, J. Geophys. Res., **64,** 1959, p. 1683.
33. McIlwain, C. E., and Pizzella, G., On the Energy Spectrum of Protons Trapped in the Earth's Inner Van Allen Zone, J. Geophys. Res., **68,** 1963, p. 1811.
34. Davis, L. R., and Williamson, J. M., *Low Energy Trapped Protons*, Space Research, vol. III, edited by W. Priester, Interscience Publishers, Inc., New York, 1963.
35. Freden, S. C., and White, R. S., Particle Fluxes in the Inner Radiation Belt, J. Geophys. Res., **65,** 1960, p. 1377.
36. Naugle, J. E., and Kniffen, D. A., Flux and Energy Spectra of the Protons in the Inner Van Allen Belt, Phys. Rev. Letters, **7,** 1961, p. 3.
37. Conference on Radiation Effects in Semiconductors, J. Appl. Phys. **30,** 1959, p. 1117.
38. Watkins, G. D., and Corbett, J. W., Electron Paramagnetic Resonance of Defects in Irradiated Silicon, Disc. Faraday Soc., **31,** 1961, p. 86.
39. Peck, D. S., Blair, R. R., Brown, W. L., and Smits, F. M., Surface Effects of Radiation on Transistors, B.S.T.J. **42,** January, 1963, p. 95.
40. Mayo, J. S., Mann, H., Witt, F. J., Peck, D. S., Gummel, H. K., and Brown, W. L., The Command System Malfunction of the *Telstar* Satellite, B.S.T.J., this issue, p. 1631.
41. Hutchison, P. T., and Swift, R. A., Results of the *Telstar* Space Experiment, B.S.T.J., this issue, p. 1475.
42. Smith, K. D., Gummel, H. K., Bode, J. D., Cuttriss, D. B., Nielsen, R. J., and Rosenzweig, W., The Solar Power Plant, B.S.T.J., this issue, part 3.

43. Loferski, J. J., and Rappaport, P., The Effect of Radiation on Silicon Solar Energy Converters, RCA Review, **19,** 1958, p. 536.
44. Rosenzweig, W., Gummel, H. K., and Smits, F. M., Solar Cell Degradation under 1-Mev Electron Bombardment, B.S.T.J., **42,** March, 1963, p. 399.
45. Rosenzweig, W., Smits, F. M., and Brown, W. L., Energy Dependence of Proton Irradiation Damage in Silicon, Bull. Am. Phys. Soc., Series II, **7,** 1962.
46. Lodi, E. A., and Crowther, D. L., Some New Results from Low Energy Proton Irradiation of Silicon, Appl. Phys. Letters, **2,** 1963, p. 22.
47. Seitz, T., and Koehler, J. S., *Displacement of Atoms During Irradiation*, Solid State Physics, vol. 2, Academic Press, 1956.
48. Baicker, J. A., Flicker, H., and Vilms, J., Proton Induced Displacement in Silicon, Appl. Phys. Letters, **2,** 1963, p. 104.
49. Denney, J. M., and Downing, R. G., private communication, May, 1962.
50. Rosenzweig, W., Augustyniak, W. M., and Wright, K. A., to be published.
51. Denney, J. M., and Downing, R. G., IEEE-AIAA Photovoltaic Specialists Conference, April 1963.
52. Bemski, G., Szymanski, B., and Wright, K. A., A New Paramagnetic Center in Electron Irradiated Silicon, J. Phys. Chem. Solids, **24,** 1963, p. 1.
53. Heppner, J. P., *The World Magnetic Survey*, Space Science Reviews, D. Reidel Publishing Company, Dordrecht, to be published.